TOPICAL REVIEW • OPEN ACCESS

Silicon-organic hybrid photonics: an overview of recent advances, electro-optical effects and CMOS integration concepts

To cite this article: Patrick Steglich *et al* 2021 *J. Phys. Photonics* **3** 022009

View the article online for updates and enhancements.

Journal of Physics: Photonics

TOPICAL REVIEW

Silicon-organic hybrid photonics: an overview of recent advances, electro-optical effects and CMOS integration concepts

Patrick Steglich[1,2,*] ⓘ, Christian Mai[1], Claus Villringer[2], Birgit Dietzel[2], Siegfried Bondarenko[2], Viachaslau Ksianzou[2], Francesco Villasmunta[1,2,3], Christoph Zesch[2], Silvio Pulwer[2], Martin Burger[2], Joachim Bauer[2], Friedhelm Heinrich[2], Sigurd Schrader[2], Francesco Vitale[3], Fabio De Matteis[3], Paolo Prosposito[3], Mauro Casalboni[3] and Andreas Mai[1,2]

[1] IHP—Leibniz-Institut für innovative Mikroelektronik, Im Technologiepark 25, D-15236 Frankfurt (Oder), Germany
[2] Technical University of Applied Sciences Wildau, Hochschulring 1, D-15745 Wildau, Germany
[3] University of Rome 'Tor Vergata', Department of Industrial Engineering, I-00133 Rome, Italy
[*] Author to whom any correspondence should be addressed.

E-mail: steglich@ihp-microelectronics.com

Abstract

In recent decades, much research effort has been invested in the development of photonic integrated circuits, and silicon-on-insulator technology has been established as a reliable platform for highly scalable silicon-based electro-optical modulators. However, the performance of such devices is restricted by the inherent material properties of silicon. An approach to overcoming these deficiencies is to integrate organic materials with exceptionally high optical nonlinearities into a silicon-on-insulator photonic platform. Silicon–organic hybrid photonics has been shown to overcome the drawbacks of silicon-based modulators in terms of operating speed, bandwidth, and energy consumption. This work reviews recent advances in silicon–organic hybrid photonics and covers the latest improvements to single components and device concepts. Special emphasis is given to the in-device performance of novel electro-optical polymers and the use of different electro-optical effects, such as the linear and quadratic electro-optical effect, as well as the electric-field-induced linear electro-optical effect. Finally, the inherent challenges of implementing non-linear optical polymers on a silicon photonic platform are discussed and a perspective for future directions is given.

1. Introduction

With the fast evolution of data traffic in worldwide communication networks, the microelectronic industry requires significant advancements in chip-integrated communication systems. Photonic integrated circuits based on silicon-on-insulator (SOI) technology have attracted increasing research interest and play a major role in this development [1]. SOI technology provides the ability to fabricate silicon photonic devices together with electronic devices on a single chip [2–5]. The integration of photonic devices on SOI substrates has reached industrial standards due to substantial research investment [6–8]. Today, complementary-metal-oxide-semiconductor (CMOS) fabrication methods are used to produce photonic integrated circuits at the wafer level. Therefore, photonic integrated circuits will play an omnipresent role, impacting such areas as high-speed communications for mobile devices, optical communication within computers, and data centers, and within sensor systems for medical applications [7, 9–14]. Ongoing research aims to increase data rates with high signal quality while reducing the associated energy consumption [15].

In general, electro-optical (EO) signal modulation is the key function in many types of telecommunication devices. In the case of silicon-based systems, one can distinguish between two major groups of EO modulators, classified by their material systems. The first relies on the plasma dispersion effect of silicon itself [15], while the second relies on the non-linear properties of a hybrid integrated material on

silicon that provides a strong Pockels (linear EO) or Kerr (quadratic EO) effect [16]. Silicon-based modulators consist of silicon waveguides, which are typically doped in such a way that they form either a pn-diode or a pin-diode. By applying a voltage to the waveguide, the optical properties of the waveguide are changed. EO modulators employ this effect to modulate light in dependence on an applied driver voltage. Fundamental speed limitations are related to carrier transport mechanisms (injection and removal of carriers). Therefore, parametric processes are impaired by nonparametric processes such as two-photon absorption, which become the main limiting factor. Moreover, silicon suffers from a linear EO effect and, as a consequence, detrimental coupling of the amplitude and phase of the guided optical wave [17]. This makes higher modulation formats challenging to realize and usually leads to relatively high energy consumption. Therefore, recent research has focused on the hybrid integration of a second material system, e.g. III–V compounds [18], lithium niobate thin films [19], barium titanate [20], phase-change materials [21], or organic EO materials [22]. The latter is within the scope of this review.

Silicon–organic hybrid (SOH) photonics, i.e. the combination of silicon photonics with functionally optimized organic EO materials, offers an approach to solving these problems [23, 24]. SOH photonics is a viable extension of SOI technology. In recent years, there has been an increasing interest in SOH photonics, mainly supported by two developments. First, increasingly rapid advances in the field of organic EO materials have been accomplished in the past thirty years, leading to remarkable non-linear optical properties [25, 26]. Second, an innovative silicon waveguide structure, known as slot waveguide, was introduced in 2004 [27, 28]. This waveguide structure fits very well with the use of photonics SOI platforms.

Organic materials exhibit off-resonant EO properties allowing for the manipulation of the amplitude and phase of the optical carrier wave independently of each other using an interferometric configuration. Thus, they enable the realization of higher modulation formats and high-bit-rate data transmission. Moreover, such SOH modulators are extremely energy-efficient and can overcome the limitations of current silicon-based modulators [29] because the electric field is sufficient to change the refractive index without carrier injection. This minimizes carrier transport and reduces the device's capacitance, a major cause of the relatively high energy consumption of currently established EO modulators.

Potential applications that can be enabled by SOH photonics are: high-speed modulators with ultra-low energy-consumption [29], frequency combs featuring flat-topped spectra [30, 31], tunable optical filters exhibiting ultra-high wavelength tuning [32], non-linear optical devices for frequency doubling [33], and laser sources [34]. The nonlinear optical properties of organic materials [35], and the simultaneous use of linear and quadratic EO effects [36] also offer perspectives for novel device concepts for programmable photonics [37].

This paper reviews the recent advances in SOH photonics based on SOI technology with a special emphasis on the in-device performance of EO polymers, and reports on the latest developments of SOH key-components such as slot waveguides and strip-to-slot mode converters. It is mainly devoted to the following aspects: (a) advances in SOH device concepts and the operating principles of SOH devices, (b) in-device performance of EO polymers, and (c) an overview of CMOS integration concepts.
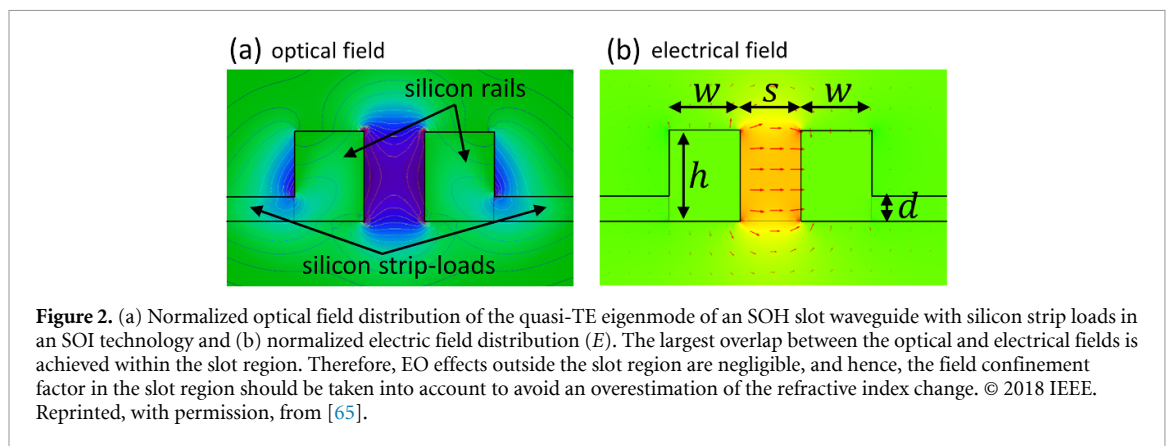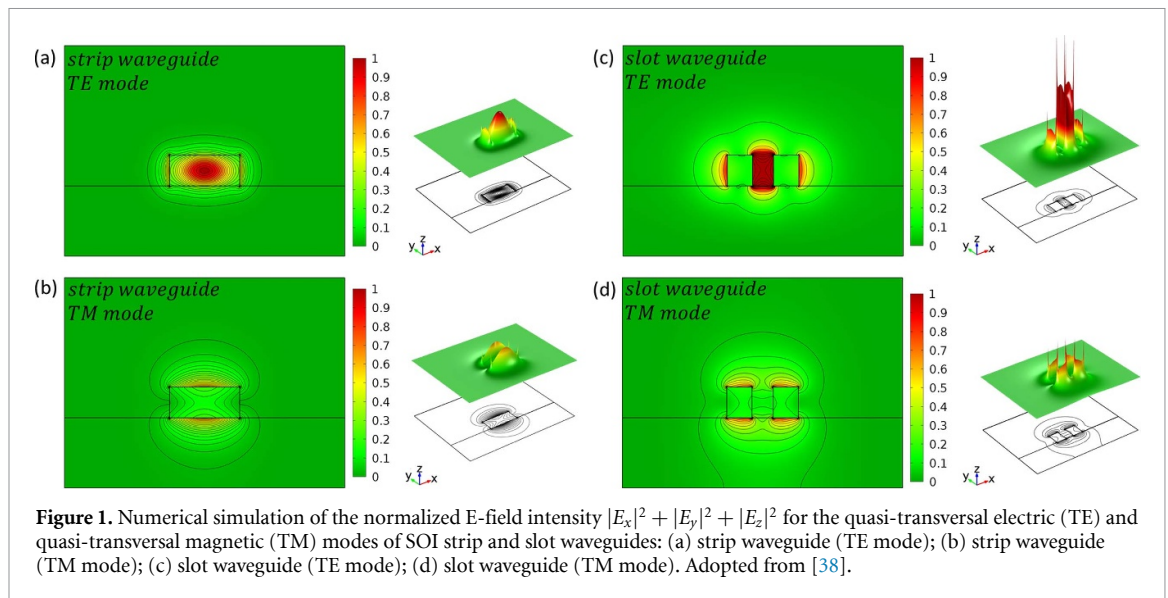
2. Advances in SOH device concepts

2.1. Slot waveguide

The concept of the slot waveguide plays a key role in SOH photonics. Almeida *et al* [27] proposed this novel waveguide structure in 2004 and Xu *et al* [28] provided the first experimental proof in the same year. A SOI slot waveguide consists of two silicon rails separated by a sub-wavelength distance. A comprehensive study of SOI slot waveguide structures can be found in [38]. Figure 1 shows a comparison between the optical field distribution in a common strip waveguide and that of a slot waveguide. As can be seen from this figure, the light is mainly confined in the high-index silicon strip waveguide, while for slot waveguides the light is mainly in the cladding material between the two silicon rails, making an efficient interaction between the guided light and the non-linear optical cladding material feasible.

Electrical connections to the two walls of the slot waveguide are necessary to perform modulation of the light, meaning that doped silicon has to be used, as illustrated in figure 2, where optical 2(a) and electrical 2(b) field distributions are depicted.

The main advantage of slot waveguides lies in the previously mentioned high field confinement inside the slot, which leads to a strong interaction between the guided light and the interposed cladding material (EO polymer). In recent years, there has been an increasing amount of literature concerning the field confinement in slot waveguides aimed at improving the waveguide geometry for EO applications [39–43]. Several studies have revealed that it is not just the slot width, s, that influences the field confinement but also the rail width, w. The optimized field-confinement factor inside the slot of a vertical silicon slot waveguide fabricated using

Figure 1. Numerical simulation of the normalized E-field intensity $|E_x|^2 + |E_y|^2 + |E_z|^2$ for the quasi-transversal electric (TE) and quasi-transversal magnetic (TM) modes of SOI strip and slot waveguides: (a) strip waveguide (TE mode); (b) strip waveguide (TM mode); (c) slot waveguide (TE mode); (d) slot waveguide (TM mode). Adopted from [38].

Figure 2. (a) Normalized optical field distribution of the quasi-TE eigenmode of an SOH slot waveguide with silicon strip loads in an SOI technology and (b) normalized electric field distribution (E). The largest overlap between the optical and electrical fields is achieved within the slot region. Therefore, EO effects outside the slot region are negligible, and hence, the field confinement factor in the slot region should be taken into account to avoid an overestimation of the refractive index change. © 2018 IEEE. Reprinted, with permission, from [65].

SOI technology is about 0.2; i.e. only $\approx$20% of the guided light interacts with the EO polymer and the applied electric field. However, the relatively large overlap between the electric and optical fields leads to an efficient phase shift of the guided light. A more comprehensive study of the field confinement factor of SOI slot waveguides can be found in [44].

In recent years, slotted photonic crystal waveguides have been demonstrated to be appropriate candidates for use in SOH photonics [45–50]. Slotted photonic crystals allow for slow light propagation and strong field confinement, enabling efficient EO modulation [51, 52], and can form a resonator by employing different photonic crystal dimensions along the length of a slot waveguide [53, 54], as shown in figure 3. The resonator is defined by the cavity region (PhC1) and the reflector (PhC2). An injector section (PhC3) between PhC2 and the slot waveguide is implemented for low-loss light coupling.

The main drawback of slot waveguides is the relatively large optical loss caused by sidewall roughness. Slot waveguides typically have propagation losses of around 4 dB mm^{-1} [55], while slotted photonic crystal waveguides show even higher losses of 15 dB mm^{-1} for 1D photonic crystal slot waveguides [56] and 20 dB mm^{-1} for 2D photonic crystal slot waveguides [57]. In the case of slotted photonic crystal waveguides, a record low propagation loss of 5.1 dB mm^{-1} has been demonstrated by introducing the photonic crystal structure inside the slot [58]. However, a promising approach for tackling the general issue of high propagation loss in slot waveguides is to cover the slot waveguide with an atomic layer of a thin dielectric film, e.g. amorphous titanium dioxide (TiO_2), thereby reducing the propagation loss to 7 dB cm^{-1} [59–62]. However, the additional atomic layer can also be used to reduce the slot width, s. For example, a slot width of about 34 nm was demonstrated using atomic layer deposition of Al_2O_3 [63]. Additionally, gold can subsequently be deposited, to further reduce the gap to 15 nm, which eventually creates a plasmonic structure. Although the atomic layer deposition of TiO_2 or Al_2O_3 reduces the propagation loss and slot width, it is associated with additional and cost-inefficient production steps, which makes it rather unattractive from a commercial point of view. The most recent advances in waveguide production, however, have led to the reduction of losses to as little as 3.7 dB cm^{-1} without atomic layer deposition [64]. In this

Figure 3. A slotted photonic crystal (PhC) waveguide structure, forming a resonator for EO modulators. Adopted from [53], © 2009 Optical Society of America.

Figure 4. (a) Direct mode-coupler strip-to-slot mode converter. (b) Gradual waveguide taper strip-to-slot mode converter. Adopted from [71].
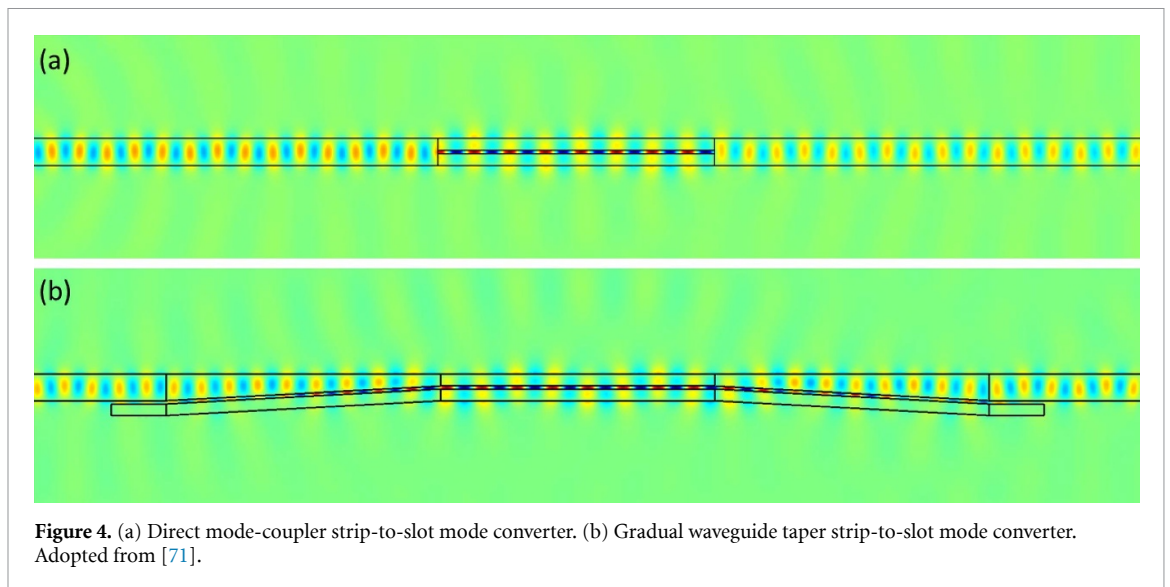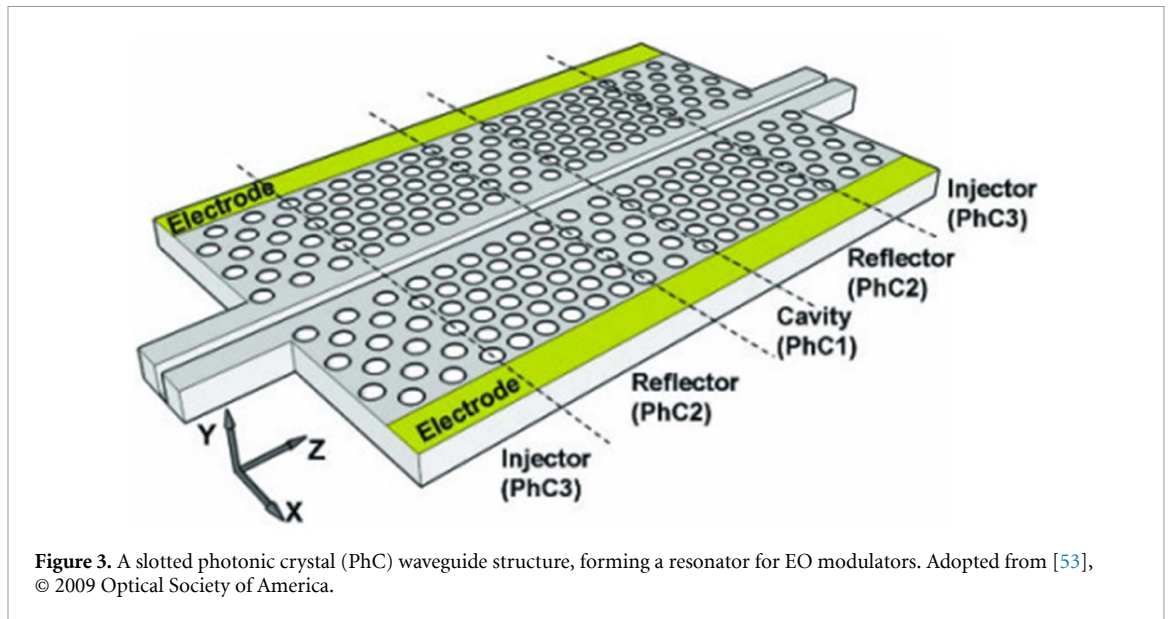
case, to reduce sidewall roughness, a tetramethylammonium hydroxide-based anisotropic wet-etching technique was applied following waveguide fabrication using e-beam lithography and a dry-etch process.

2.2. Strip-to-slot mode converter

To minimize the optical losses of a device, it is convenient to make the region of the waveguide containing the slot as short as possible. This implies that particular attention must be paid to strip-to-slot mode conversion, which plays a vital role in SOH photonics. Strip-to-slot mode converters are designed to achieve a smooth transition between strip and slot waveguides. An efficient strip-to-slot waveguide transition is needed to exploit the advantages of both strip and slot waveguides, and to combine them in a single device or circuit. Strip-to-slot mode converters can be achieved by either implementing a slowly varying waveguide taper [66–68] or a direct mode coupler [69, 70].

Direct strip-to-slot mode converters permit a highly compact solution and have been demonstrated to offer efficient modal coupling. Figure 4(a) shows a numerical simulation of a simple direct mode converter. Typical loss values of about 0.91 dB can be achieved for such a direct strip-to-slot mode converter, as experimentally shown in [70]. Since the conversion efficiency is only adequate at narrow slot widths, i.e. <50 nm, due to the back reflection of light, such direct couplers are not appropriate for optical switching. This is because the light–matter interaction described by the field confinement factor decreases with decreasing slot width. However, an improved direct mode converter based on symmetric multimode interference was presented by Deng *et al* [72]. This mode converter achieved a measured efficiency of 97%. In
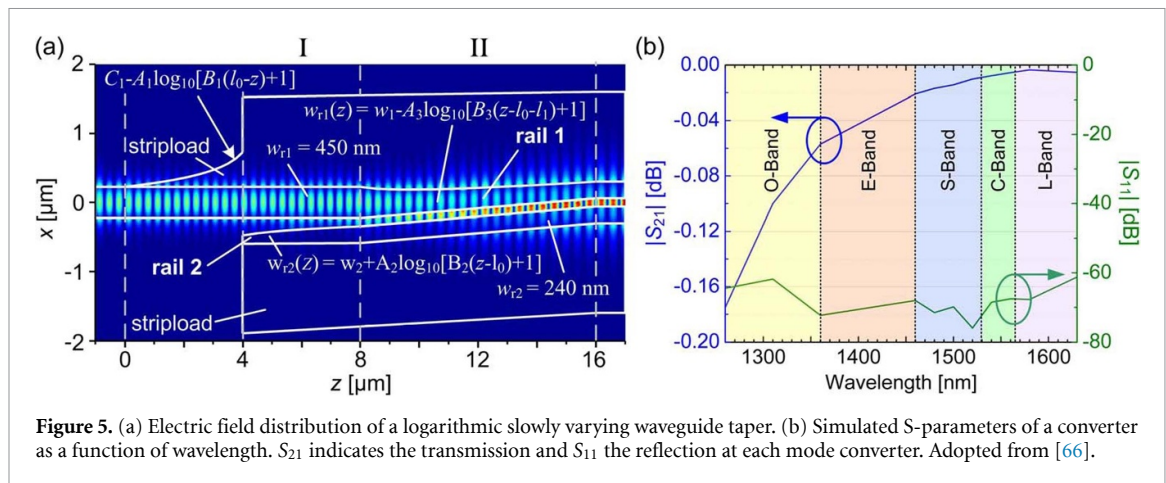
Figure 5. (a) Electric field distribution of a logarithmic slowly varying waveguide taper. (b) Simulated S-parameters of a converter as a function of wavelength. S_{21} indicates the transmission and S_{11} the reflection at each mode converter. Adopted from [66].

2016, Deng *et al* [69] expanded this concept to obtain a polarization-insensitive direct mode converter. Measured conversion efficiencies of 95.9% for TE_0 and 96.6% for TM_0 were achieved. More recently, another innovative direct mode converter was presented by Mere *et al* [73]. Their mode converter consisted of a balanced 50/50 power splitter and a tunable phase-matched taper combiner forming a slot waveguide. They experimentally demonstrated a coupling efficiency of 99%.

One drawback of direct mode converters is that they are not usable in EO phase shifters because the silicon rails are connected to each other, and they form an electric conductor, making electric field generation impossible. In this case, slowly varying waveguide tapers are preferred for EO modulators. A numerical simulation of such a mode converter is shown in figure 4(b). As can be seen from this figure, the upper silicon rail is separated from the lower one. Consequently, this type of mode converter forms a capacitor when a voltage is applied to the silicon rails. In 2011, Yang Liu *et al* published a paper in which they described a mode converter based on a slowly varying waveguide taper with losses of around 0.81 dB [67]. In 2013, Palmer *et al* investigated the same type of mode converter and achieved record low losses of about 0.02 dB and negligible reflections between 1480 and 1580 nm [66]. This was achieved by the use of a logarithmic slowly varying waveguide taper instead of a linear one, as shown in figure 5.
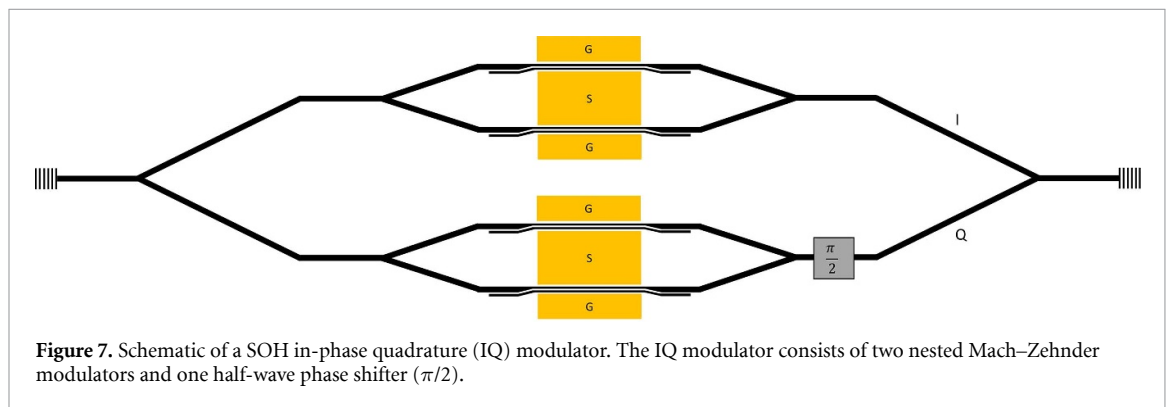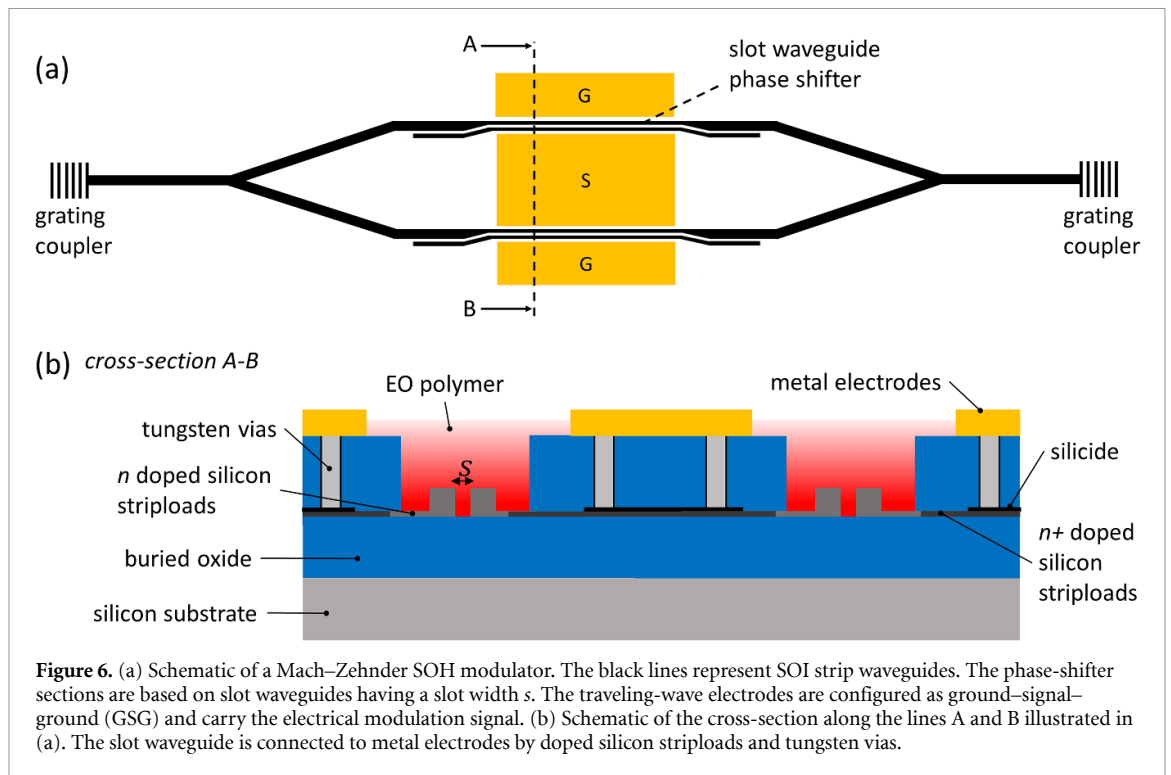
2.3. Mach–Zehnder interferometer

A schematic representation of a SOH Mach–Zehnder interferometer is shown in figure 6. Mach–Zehnder interferometers are composed of either one Y-splitter and one Y-combiner, or of a 1×2 multimode interference (MMI) splitter and a 2×1 MMI combiner. The slot waveguide is electrically connected, so that a ground–signal–ground (GSG) coplanar traveling-wave electrode configuration with a 50 ohm termination is realized for push-pull operation. The slot waveguide is infiltrated with an EO polymer and serves as an active phase shifter. In this way, ultra-compact SOH Mach–Zehnder modulators with slot waveguide lengths as low as 500 μm were demonstrated [74]. However, typical slot waveguide lengths range from 1 to 2 mm.

SOH Mach–Zehnder modulators benefit from the off-resonant Pockels effect, making higher modulation formats feasible. In particular, *IQ*-modulators have been demonstrated by combining two SOH Mach–Zehnder modulators, as schematically shown in figure 7. Here, *I* stands for the in-phase and *Q* for the quadrature component. During the last decade, several SOH Mach–Zehnder modulators have been demonstrated to operate at 10 Gbit s^{-1} [29], 12.5 Gbit s^{-1} [75], 40 Gbit s^{-1} [23], 84 Gbit s^{-1} [76], 100 Gbit s^{-1} [77], 112 Gbit s^{-1} [78] and 120 Gbit s^{-1} [79] and advanced modulation formats such as 16QAM (quadrature amplitude modulation) [75] as well as OOK (on–off keying), BPSK (binary phase-shift keying), 8-ASK (amplitude-shift keying with 8-binary symbols) [80] and PAM4 (four-level pulse-amplitude modulation) [77, 79] signals have also been demonstrated. These results suggest that SOH phase shifters enable higher-order modulation formats without compromising on signal quality, and therefore have high potentiality in the field of communication systems.

The voltage-length product is a figure of merit that can be used to compare state-of-the-art phase shifters based on SOH slot waveguides with depletion-type phase shifters. It is often used in the literature to characterize the effectiveness of phase-shifters. It is defined as the voltage U_π needed to induce a phase shift of π multiplied by the phase shifter's length, which is just the slot waveguide's length L_{slot} [81].

There are several publications targeting low voltage-length products by the use of Mach–Zehnder interferometers [77, 79, 82–84]. In 2014, Lauermann *et al* [85] experimentally showed a SOH Mach–Zehnder modulator with a voltage–length product of only 0.53 V mm and an energy consumption of less than 19 fJ bit^{-1}.

Figure 6. (a) Schematic of a Mach–Zehnder SOH modulator. The black lines represent SOI strip waveguides. The phase-shifter sections are based on slot waveguides having a slot width *s*. The traveling-wave electrodes are configured as ground–signal–ground (GSG) and carry the electrical modulation signal. (b) Schematic of the cross-section along the lines A and B illustrated in (a). The slot waveguide is connected to metal electrodes by doped silicon striploads and tungsten vias.

Figure 7. Schematic of a SOH in-phase quadrature (IQ) modulator. The IQ modulator consists of two nested Mach–Zehnder modulators and one half-wave phase shifter ($\pi/2$).

2.4. Ring resonators

High-performance EO modulators based on SOH photonics have mostly been demonstrated using Mach–Zehnder interferometers. On the one hand, these modulators are appropriate candidates for the generation of higher-order modulation formats, but, on the other hand, their large footprint represents a substantial limitation, resulting in a large areal consumption on the chip and a high insertion loss. To overcome these restrictions, a different modulator geometry has been proposed, namely optical ring resonators, as shown in figure 8(a). Indeed, ring resonators are applicable as EO modulators as well as for tunable filters and switches. They are significantly smaller, which is of great benefit in achieving high integration densities, low optical losses, and low energy consumption.

Only a few SOH ring resonator modulators have been described that used SOI technology . The main reason for this is that SOI slot waveguides suffer from relatively high losses. This is mainly caused by sidewall roughness [87]. As a consequence, slot waveguide resonators such as micro-ring resonators typically have small optical quality factors (Q-factors) [88–90]. One possible approach to tackle this problem is to reduce propagation losses in slot waveguides by atomic layer deposition, as described in the previous section. However, a slot waveguide ring resonator modulator having a 6 dB bandwidth of 1 GHz, a device tunability of 12.7 pm V^{-1}, and a Q-factor of 5000 was demonstrated in 2011 [88]. Furthermore, a double-slot waveguide ring resonator covered by liquid crystal was proposed and theoretically analyzed to have a device tunability of 81.4 pm V^{-1}, but was never realized in practice [91]. In 2016, Weiwei *et al* [92, 93] demonstrated that it is possible to improve the Q-factor from 3000 to 30 600 by optimizing the coupling conditions.
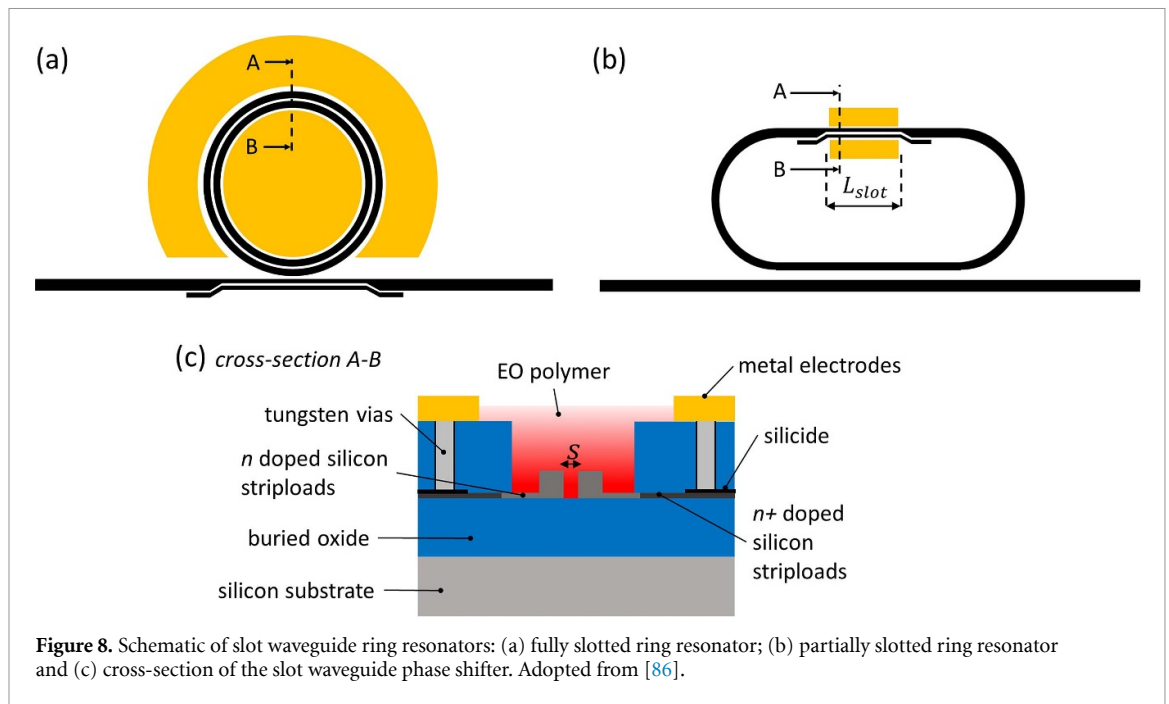
Figure 8. Schematic of slot waveguide ring resonators: (a) fully slotted ring resonator; (b) partially slotted ring resonator and (c) cross-section of the slot waveguide phase shifter. Adopted from [86].

An alternative strategy consists of exploiting the concept of a partially slotted ring resonator [94]. Here, a slot waveguide is inserted into one of the straight sections of an elongated ring resonator (also called a racetrack resonator), as shown in figure 8(b). This partially slotted ring resonator concept is a promising candidate for integrating a SOH phase shifter into a ring resonator, keeping the optical loss at a very low value. An extremely high device tunability of 700 pm V^{-1} was demonstrated using such a ring resonator covered by a side-chain polymer system (poly[(methyl methacrylate)-co-(disperse red 1 acrylate)]) [32]. A second advantage of this ring configuration is the reduced capacitance, which allows for an ultra-low energy per-bit consumption of 87 aJ per bit [65]. Also, a 3 dB bandwidth at 1.34 GHz has been demonstrated, giving rise to RF (radio frequency) modulators with low energy consumption.

A second promising ring concept is based on subwavelength grating waveguides (SWG) [95–98]. Here, the slot is introduced orthogonally to the direction of light propagation, instead of being parallel to it, as it is usually realized. In 2018, Pan *et al* [99] demonstrated this concept to be appropriate for an EO modulator with a 3 dB modulation bandwidth as high as 41.4 ± 1.1 GHz, while the device footprint was as small as 70 μm $\times$ 29 μm [95]. A device tunability of 41.28 pm V^{-1} was deduced from DC measurements. The difference between the high tunability of a partially slotted ring resonator and the SWG is the fact that the SWG-based ring resonator exhibits a significantly larger electrode gap. Figure 9 shows a schematic of an SWG-based ring resonator, which has a racetrack configuration.
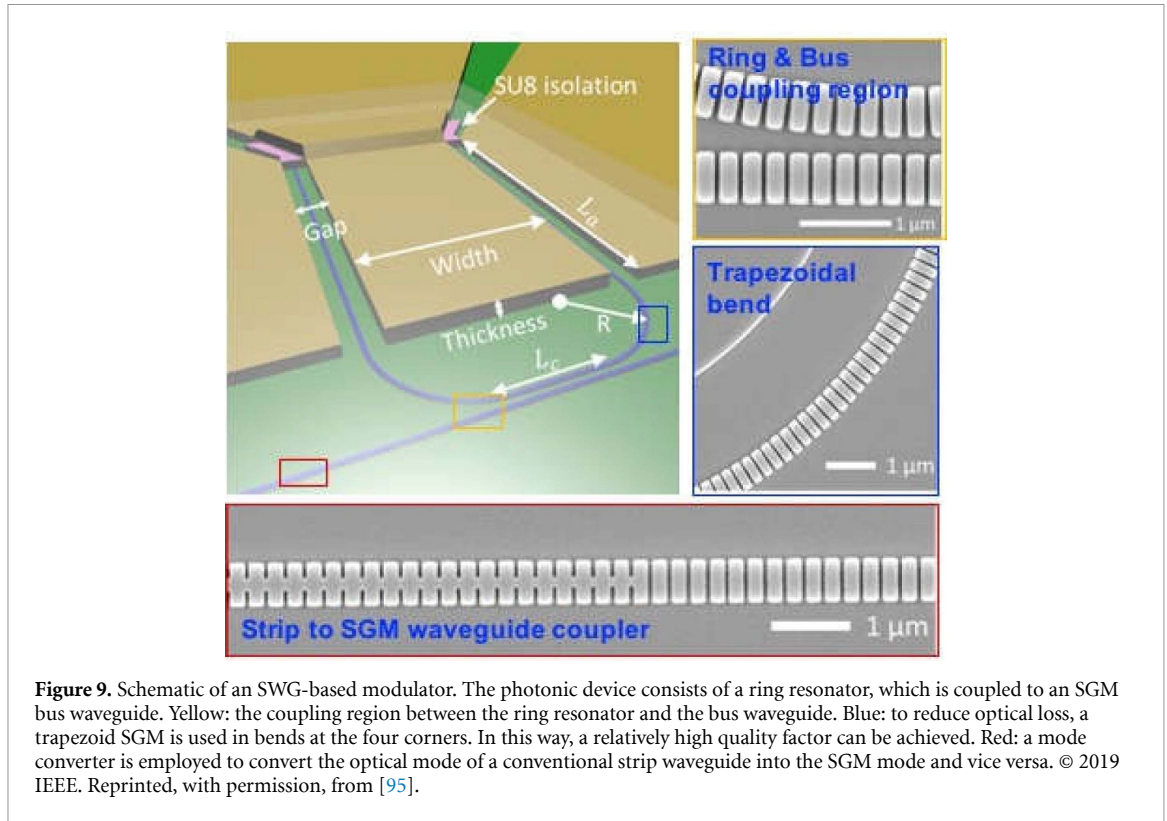
3. In-device performance of electro-optical polymers

3.1. Electro-optical effects in silicon-organic hybrid devices
In general, an EO polymer consists of a passive matrix containing active molecules with a strong EO effect. The polymeric matrix gives the material its mechanical, thermal and chemical stability. In principle, active molecules can be endowed with both linear and quadratic EO properties that can produce changes in refractive index through the application of an electric field.

Most EO devices based on organic linear EO materials rely on dipolar molecules embedded in, or covalently bound to, the main chains of a usually amorphous polymer matrix. To act as a modulator under the application of an external electric field E, a macroscopic non-centrosymmetric orientation of the dipolar molecules has to be generated using an appropriate poling procedure [100]. The refractive index varies linearly with the electric field E and the lack of inversion symmetry allows $\Delta n(-E) \neq \Delta n(E)$. This leads to a linear EO (or Pockels) effect, which is appropriate for high-frequency application. However, the poling procedure is sophisticated and prone to thermal instability and the reproducibility of the result is inadequate for industrial applications. In spite of this, a huge amount of literature is available, on both the materials and the devices [101–113].

To overcome the intrinsic issues due to the linear EO effect, materials with a quadratic dependence of the refractive index on the electric field can be exploited. In this case, no requirement of symmetry is necessary,

Figure 9. Schematic of an SWG-based modulator. The photonic device consists of a ring resonator, which is coupled to an SGM bus waveguide. Yellow: the coupling region between the ring resonator and the bus waveguide. Blue: to reduce optical loss, a trapezoid SGM is used in bends at the four corners. In this way, a relatively high quality factor can be achieved. Red: a mode converter is employed to convert the optical mode of a conventional strip waveguide into the SGM mode and vice versa. © 2019 IEEE. Reprinted, with permission, from [95].

because Δn depends on E^2. All materials have a quadratic EO response; however, it is much smaller than the linear response for non-centrosymmetric systems.

The linear and quadratic EO effects have been intensively studied in bulk materials during recent decades. Typically, each effect is considered separately, because the linear EO effect dominates in non-centrosymmetric materials and vanishes in centrosymmetric materials. However, attention is required when EO polymers are used in slot waveguides with narrow gaps (below 200 nm), as is typical for SOH photonics. It has been shown that the quadratic EO effect has a noticeable contribution to the overall EO effect, even in non-centrosymmetric materials [36]. Therefore, it is necessary to take both effects into account.

The microscopic polarization induced by an electric field can be described in terms of a Taylor series. This leads to the field-dependent molecular dipole moment [114]:

$$p_i = \mu_i + \alpha_{ij}E_j + \beta_{ijk}E_jE_k + \gamma_{ijkl}E_jE_kE_l + \dots, \tag{1}$$

where μ_i is the static electric dipole moment, α_{ij} is the first-order polarizability, β_{ijk} is the second-order polarizability, and γ_{ijkl} is the third-order polarizability. Note that this total dipole moment p_i, taken per average molecular volume, represents the molecular polarisation. E_j, E_k and E_l are the electric field components. The higher-order polarizabilities in this series have also been called first- and second-hyperpolarizability, respectively.

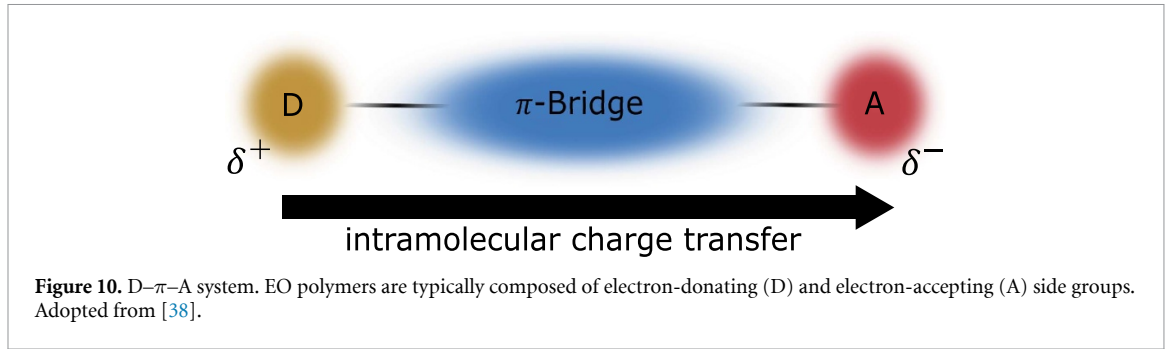The EO effect is usually described using the change of the optical indicatrix [115]:

$$\Delta\left(\frac{1}{n^2}\right)_{ij} = r_{ijk}E_k + R_{ijkl}E_kE_l, \tag{2}$$

where r_{ijk} and R_{ijkl} are the Pockels and Kerr coefficients, respectively, which describe the linear and quadratic EO effects. In anisotropic materials and presuming a small change of the refractive index, the refractive-index change Δn_i in the main direction of the optical indicatrix can be approximated by [114]:

$$\Delta n_i \cong -\frac{1}{2}n_i^3\left(r_{ijk}E_k + R_{ijkl}E_kE_l\right). \tag{3}$$

The EO effect can also be expressed using the non-linear susceptibility tensors as [36, 114]:

$$\Delta n_i = \frac{1}{n_i}\left(\chi_{ijk}^{(2)}E_k + \frac{3}{2}\chi_{ijkl}^{(3)}E_kE_l\right). \tag{4}$$

Figure 10. D–π–A system. EO polymers are typically composed of electron-donating (D) and electron-accepting (A) side groups. Adopted from [38].

For SOH photonics, the special case of $i = j = k = l = 3$ is of particular interest in slot-waveguide structures. This is because it represents the dominant tensor components $\chi^{(2)}_{333}$ and $\chi^{(3)}_{3333}$, where both input fields, i.e. the optical and electrical fields, are polarized along axis 3. Therefore, this notation will be used throughout this work. Further, we assume an isotropic refractive index, which is referred to as n. The EO tensors r_{ijk} and R_{ijkl} are related to the second- and third-order susceptibility coefficients $\chi^{(2)}_{ijk}$ and $\chi^{(3)}_{ijkl}$, respectively. Comparing equations (3) and (4) yields the classical relations [36]:

$$r_{ijk} = -\frac{2\chi^{(2)}_{ijk}}{n_i^2 n_j^2},\tag{5}$$

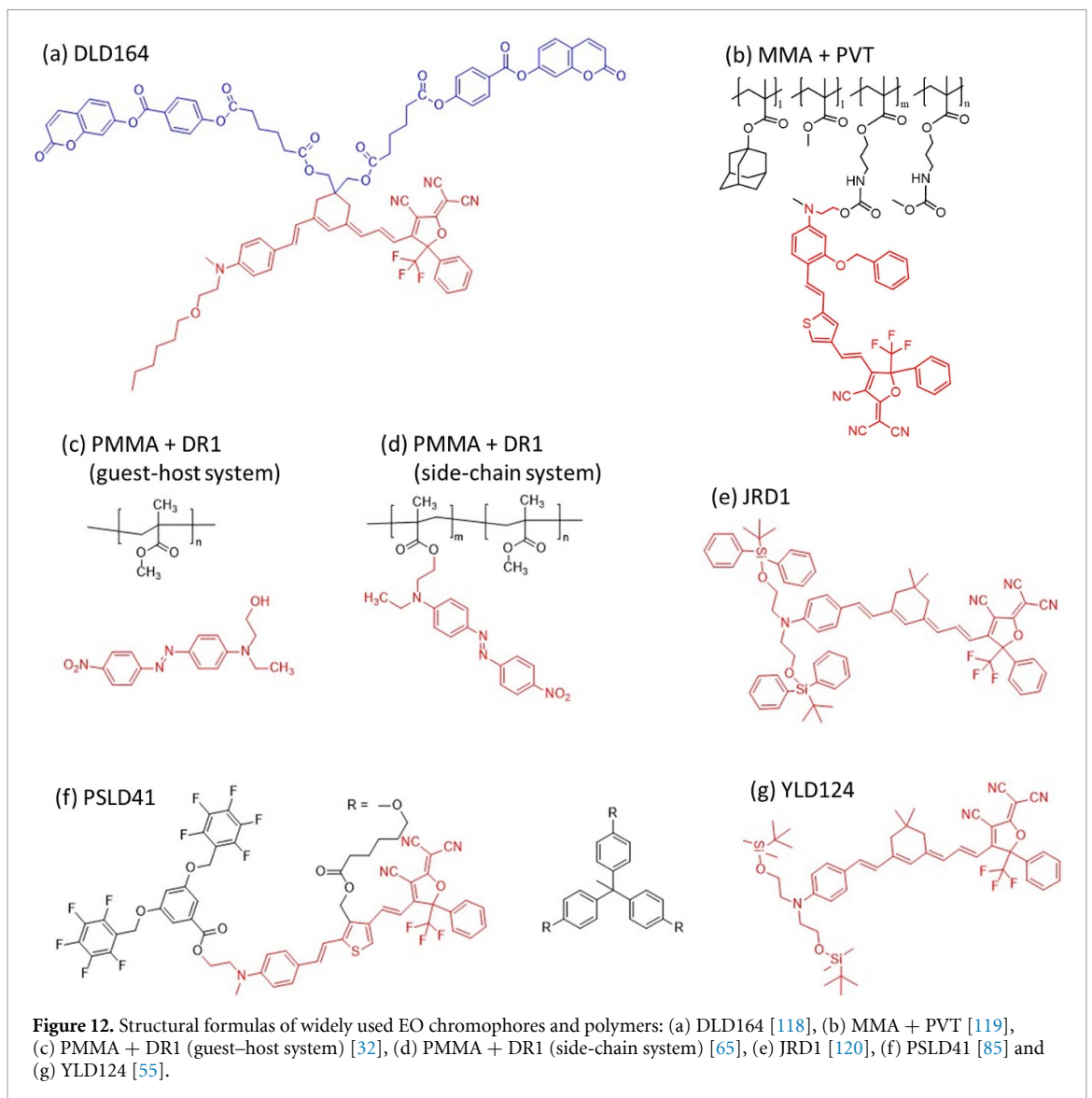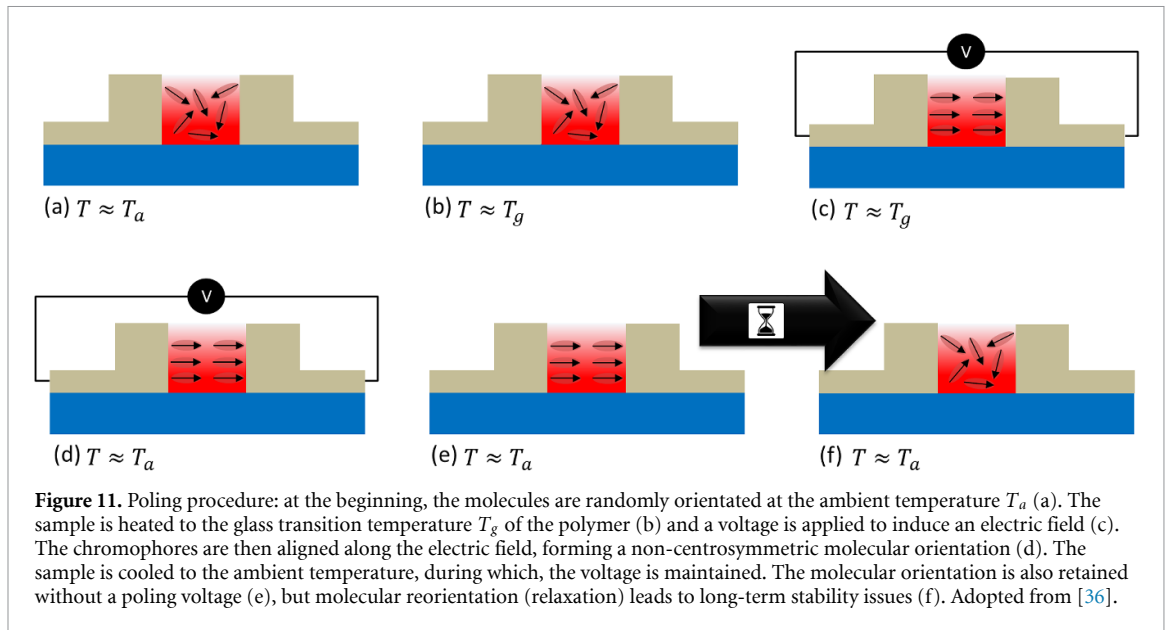$$R_{ijkl} = -\frac{3\chi^{(3)}_{ijkl}}{n_i^2 n_j^2}.\tag{6}$$

3.2. In-device performance of the linear electro-optical effect

The linear EO tensor r_{ijk} describes the EO activity of a non-centrosymmetric material and can be represented in the case of guest–host systems by [114]:

$$r_{ijk} \propto N\beta\langle\cos^3\Theta\rangle.\tag{7}$$

In equation (7), the chromophore number density or the number of non-linear molecules in the material contributing to the polarization are denoted as N, and β represents the molecular first hyperpolarizability. The average non-centrosymmetric order parameter is given by $\langle\cos^3\Theta\rangle$, where Θ denotes the angle between the molecular dipole's axis and the electric field vector. Equation (7) suggests that three approaches to increase the linear EO effect are possible: (a) first, increasing the chromophore number density N; (b) second, using chromophores with high first hyperpolarizability β; (c) third, maximizing the average non-centrosymmetric order parameter $\langle\cos^3\Theta\rangle$ by inducing a high molecular orientation. EO polymers that are dipolar and exhibit a highly polarizable donor–π–acceptor (D–π–A) system can meet such requirements. In general, the D–π–A system can support charge transfer between electron-donating and electron-accepting groups [116]. The electron donor groups mainly used in organic synthesis, are usually $N(CH_3)_2$, OCH_3, OH, while the electron acceptor groups are mostly NO, O_2N, CHO, CN. The π–electron conjugated segment serves to transmit the charge, as illustrated in figure 10. A poling procedure is required to obtain a non-centrosymmetric molecular orientation and, hence, a large linear EO coefficient r_{33}. In principle, the procedure is as follows. First, the sample is heated from the ambient temperature (figure 11(a)) to nearly the glass transition temperature of the polymer (figure 11(b)). Then, a relatively high voltage is applied to the slot waveguide for several minutes (figure 11(c)). The electric field usually reaches a value in the order of 200 V μm^{-1}. This phase is followed by rapid cooling to ambient temperature while the poling voltage continues to be applied (figure 11(d)). Finally, the active chromophores are aligned and fixed in their orientation so that the poling voltage can be switched off (figure 11(e)). In principle, a further increase of the EO effect in polymer systems with a non-centrosymmetric molecular orientation can be achieved by operating them near to their absorption resonances, to make use of the so-called resonance enhancement of the second-order effect [117]. A selection of widely used EO chromophores and polymers with a large linear EO effect is shown in figure 12.

    Pan *et al* demonstrated a high-speed modulator based on the EO polymer SEO125. An EO coefficient r_{33} of 54.7 pm V^{-1} was deduced from DC experiments. This, however, corresponds to a poling efficiency of only 43.8%, compared to the EO coefficient of the bulk EO polymer [95]. Further optimization of the poling process is expected to improve this value.

Figure 11. Poling procedure: at the beginning, the molecules are randomly orientated at the ambient temperature T_a (a). The sample is heated to the glass transition temperature T_g of the polymer (b) and a voltage is applied to induce an electric field (c). The chromophores are then aligned along the electric field, forming a non-centrosymmetric molecular orientation (d). The sample is cooled to the ambient temperature, during which, the voltage is maintained. The molecular orientation is also retained without a poling voltage (e), but molecular reorientation (relaxation) leads to long-term stability issues (f). Adopted from [36].

Figure 12. Structural formulas of widely used EO chromophores and polymers: (a) DLD164 [118], (b) MMA + PVT [119], (c) PMMA + DR1 (guest–host system) [32], (d) PMMA + DR1 (side-chain system) [65], (e) JRD1 [120], (f) PSLD41 [85] and (g) YLD124 [55].

One serious problem of the linear EO effect is its thermal and long-term stability due to orientational relaxation dynamics (figure 11(f)) [101, 121]. However, recent advances in molecular engineering have led to increased stability. For example, a cross-linkable EO system consisting of two chromophores (HLD_1 and HLD_2) has been demonstrated to maintain 99% of the initial r_{33} after being heated to 85 °C for 500 h, making it a promising candidate for future SOH modulators [122]. Kieninger *et al* studied a random copolymer of four differently substituted methyl-methacrylate (MMA) moieties infiltrated into a silicon slot waveguide [119]. This polymer system was introduced in 2016 [123] and exhibits a donor-acceptor-substituted phenyl vinylene thiophene (PVT) chromophore as a side group, which is responsible for the EO effect, while a bulky adamantyl side group increases the glass transition temperature. Using this polymer system, high-temperature storage experiments at 85 °C have been performed and an SOH modulator that retained more than 85% of its modulation efficiency for at least 2400 h was presented. The device had a voltage-length product of 3.3 V mm after the end of the experiment. This demonstrates the principle of the reliability of SOH modulators at elevated temperatures, which complies with Telcordia standard GR-468-CORE. However, this can only be achieved by using EO polymers with a high glass transition temperature of 172 °C [119]. In principle, the glass transition temperature needs to be significantly higher than the operating temperature to avoid relaxation processes. Unfortunately, the most active EO polymers exhibit glass transition temperatures between 80 °C and 100 °C. Therefore, a trade-off between EO activity and long-term stability is necessary. However, a temperature budget of at least 400 °C is required for the integration of organic materials into a CMOS-compatible fabrication platform due to the use of high-temperature annealing processes. To tackle this problem, novel organic EO materials have recently been synthesized that show high thermal stability at temperatures of up to 315 °C and their long term electro-optic stability has been demonstrated for 300 h at 85 °C [124].

The linear EO effect in polymers was widely used during the last decade in the development of SOH modulators, as can be seen from table 1. From this table, it is apparent that Mach–Zehnder modulators were mainly used to demonstrate high-speed modulation at line rates of up to 100 Gbit s^{-1} for OOK [77] and up to 120 Gbit s^{-1} for PAM4 signals [79]. Also, SOH modulators based on slotted photonic crystal waveguides have been demonstrated for use with EO modulation at a 40 GHz 3 dB bandwidth [54].

However, attention has to be paid to the reported r_{33} values. The reporting of reliable EO data is only possible if data analysis follows widely recognized methodologies or can be traced to accredited quantitative structure–property relationships studied by independent laboratories. There are only a few publications that provide deeper insights into the optical and EO properties of organic materials in slot waveguides. The first investigation into thin films can further help to obtain a deeper understanding [125]. However, please note that the values reported in the literature and, therefore, also in the present review, are in-device values, meaning that the EO values are deduced from the device performance, but many physical effects such as carrier accumulation or elasto-optical effects are neglected.

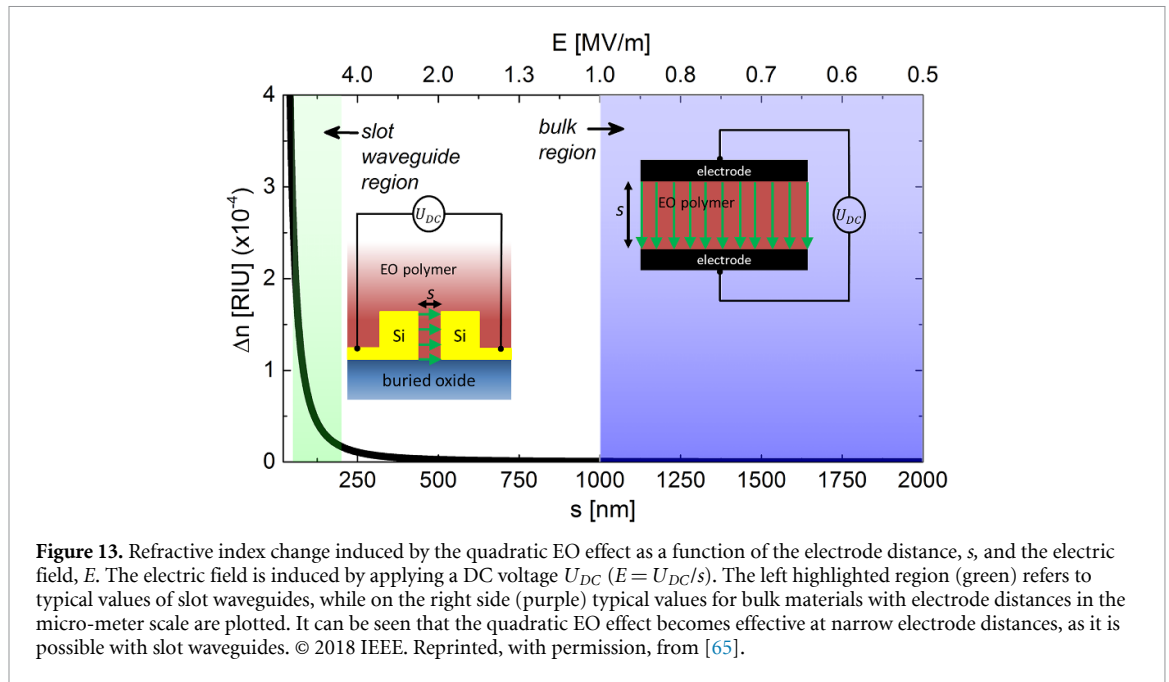### 3.3. In-device performance of the quadratic electro-optical effect

More recently, a second category of devices has emerged, relying on the quadratic EO effect in SOH slot waveguides. The quadratic EO effect is present in any molecular system irrespective of its orientation or symmetry, which is an advantage in comparison with the linear counterpart. Moreover, the combination of the quadratic EO effect with the optical Kerr nonlinearity in a slot waveguide is expected to pave the way for various applications, e.g. electrically controlled multistable switches [137]. The main issue of the quadratic EO effect is the relatively low response in terms of refractive index change as a function of the applied electric field. However, the latest research has shown the feasibility of the quadratic EO effect for low-voltage operation using an SOI slot waveguide phase shifter implemented in a micro-ring resonator [16, 86]. Due to the fact that the quadratic EO effect depends quadratically on the electrode separation, s, it becomes highly efficient in narrow slots, as plotted in figure 13.

There are several origins of the quadratic EO effect, e.g. electronic mechanisms, molecular reorientational contributions, electrode attraction, and electrostrictive effects [138]. However, electronic origins dominate the quadratic EO effect at room temperature because molecular reorientation is hindered by the restraining force of the polymer, and electrode attraction is expected to be compensated for by the elasticity of the polymer. Second-order electrostriction can be neglected in isotropic conjugated polymers, as they are centrosymmetric and have no noteworthy dipole moment [139], and third-order electrostriction is expected to have only a marginal influence. Consequently, the quadratic EO effect in conjugated polymers is dominated by electronic mechanisms, which is of great interest in photonic applications due to its exceptional bandwidth potential [140].

The main condition for a strong quadratic EO effect is that the electron system of the material should be characterized by strong confinement. One example is polydiacetylene [141, 142], preferably in crystallized

Table 1. Overview of current SOH modulators using the linear EO effect. MZ: Mach–Zehnder, RR: ring resonator, FS: frequency shifter, PM: phase shifter, OOK: on–off keying, SSB: single sideband modulation, QAM: quadrature amplitude modulation, PAM: pulse-amplitude modulation, BPSK: binary phase-shift keying, QPSK: quadrature phase-shift keying, ASK: amplitude shift keying.

Device	Polymer	r_{33} (pm V^{-1})	$U_\pi L$ (V mm)	Bandwidth (GHz)	Signal	W_{bit} (fJ bit^{-1})	Reference	Year
MZ	JRD1	—	0.41	—	100 GBd OOK and PAM4	—	[126]	2020
MZ	SEO100	166	1.1	—	100 GBd 16QAM	25	[84]	2018
RR	SEO125	54.7	—	41.4	—	2.5	[99]	2018
MZ	PVT	80	3.3	20	40 Gbit s^{-1} OOK	98	[119]	2018
MZ	SEO100	147	1.0	25	100 Gbit s^{-1} OOK	8.5	[77]	2018
MZ	JRD1	390	0.32	43	40 Gbit s^{-1} OOK	30	[127]	2018
MZ	SEO250	—	1.0	—	100 GBd 16QAM	100	[128]	2017
MZ	SEO100	144	1.1	—	120 Gbit s^{-1} PAM4	—	[79]	2017
MZ	JRD1	359	0.32	—	25 Gbit s^{-1}	—	[129, 130]	2017
MZ	SEO100	110	1.1	—	50 Gbit s^{-1} OOK, 100 Gbit s^{-1} DB	160	[131]	2017
MZ	SEO100	60	1.6	—	64 GBd 4ASK	—	[132]	2016
RR	PMMA/ DR1	12.8	—	—	—	—	[32]	2016
FS	DLD164	150	0.5	40	SSB	—	[118]	2016
PM	YLD124/ PSLD41	230	0.45	>60	40 Gbit s^{-1} BPSK	70	[133]	2015
MZ	SEO100	70	1.1	>60	40 Gbit s^{-1} OOK	225	[133]	2015
PM	M3	18	11	>100	—	—	[134]	2014
MZ	BNA	24	12	7	12.5 Gbit s^{-1} OOK	—	[78]	2014
MZ	YLD124/ PSLD41	230	1.05	18	28 GBd QPSK, 16QAM	19	[55]	2014
MZ	YLD124/ PMMA	30	4	18	40 Gbit s^{-1} OOK	—	[55]	2014
MZ	PSLD41	98	1.22	18	40 Gbit s^{-1} OOK	—	[85]	2014
MZ	YLD124/ PSLD41	230	0.52	18	40 Gbit s^{-1} OOK	—	[55]	2014
MZ	DLD-164	—	10	11	10 GBd BPSK, 2ASK-2PSK	—	[135]	2014
MZ	M3	15	2.7	10	10 Gbit s^{-1} OOK	320	[29]	2013
MZ	M3	—	1.33	6.8	28 GBd 16QAM	640	[75]	2013
MZ	M1	10	20	—	28 GBd BPSK, M-ASK	1000	[80]	2013
PM	M1	230	11	90	56 Gbit s^{-1} QPSK	<1000	[136]	2013

Figure 13. Refractive index change induced by the quadratic EO effect as a function of the electrode distance, *s,* and the electric field, *E*. The electric field is induced by applying a DC voltage U_{DC} ($E = U_{DC}/s$). The left highlighted region (green) refers to typical values of slot waveguides, while on the right side (purple) typical values for bulk materials with electrode distances in the micro-meter scale are plotted. It can be seen that the quadratic EO effect becomes effective at narrow electrode distances, as it is possible with slot waveguides. © 2018 IEEE. Reprinted, with permission, from [65].

form, aligned with the axis of the one-dimensional conjugated electron system of the polymer chains in the polarization direction of the traveling optical wave's electric field vector. Other examples are conjugated azo polymers such as poly[(methyl methacrylate)-co-(disperse red 1 methacrylate)] [65] or azo dyes such as disperse red 1 (DR1), dicyanovinyl (DCV) and nitrofuran (NFAI) [143, 144]. In principle, short conjugated oligomers and respective chromophores can also be used, e.g., beta carotene, oligoparaphenylenevinylene, and oligocyaninedyes but also more stable ladder-type polymers such as oligorylenes or ladder-type polyparaphenylene [145].

An alternative to these organic materials is represented by composite materials which are composed of a transparent dielectric matrix filled with a suitable concentration of one-dimensional conductive or semi-conducting nano-domains, which also exhibit the required confinement of the electron system. Some examples are gold, silver, tungsten, aluminum or metallic or semiconducting nanowires, and also formed and aligned nanodots which have direct contact with each other. The matrix materials can be dielectric polymers, glass or various dielectric oxides e.g. silicon dioxide or other suitable oxides e.g. hafnium dioxide. In addition, certain inorganic materials can be used, e.g. salts such as sulfides, bisphosphonates or nitrates. In this case, the crystallographic axis with the highest linear polarizability and hyperpolarizability should be aligned to a sufficient extent with the polarization direction of the electrical field used for modulation. Other promising materials are ferroelectrics such as potassium lithium tantalate niobate $K_{1-y}Li_yTa_{1-x}Nb_xO_3$ (KLTN) [146] and materials based on $CsPbBr_3$ nanocrystals [147].

Recently, the first RF modulator based on the quadratic EO effect in poly[(methyl methacrylate)-co-(disperse Red 1 methacrylate)] was demonstrated with a 3 dB bandwidth of 1.34 dB [65]. This SOH ring resonator modulator was realized using a photonic integrated circuit (PIC) technology on a 200 mm wafer, demonstrating wafer-scale fabrication of SOH devices. An exceptionally large device tunability of 350 $pm\,V^{-1}$ was achieved, surpassing state-of-the-art silicon modulators by an order of magnitude. Moreover, the ring resonator has an advanced design to obtain an ultra-low per-bit energy consumption of 87 $aJ\,bit^{-1}$. This demonstrates the potential of the quadratic EO effect to be used in high-performance photonic devices with low energy consumption.

A method for determining the dispersion of the third-order susceptibility and the molecular hyperpolarizability of a SOH slot waveguide ring resonator is presented in [86]. Here, a two-level model is used to determine the dispersion of the third-order hyperpolarizability of a linear conjugated molecule in the off-resonant spectral region (the optical C-band). Poly(methylmethacrylate) doped with 5 wt% DR1 was employed to evaluate the quadratic EO coefficients R_{11} and R_{12}. Figure 14 shows the observed quadratic EO coefficients. Note that the values of R_{11} were experimentally obtained (black dots) and fitted using a least-squares fitting procedure (red line), while the values for R_{12} were evaluated from R_{11} using the relation $R_{11} = 3R_{12}$. However, it is worth highlighting that the ring resonator used was fabricated with an SOI technology, which allowed the evaluation of the on-chip performance of novel EO materials using the same technological conditions as those used for the final device.
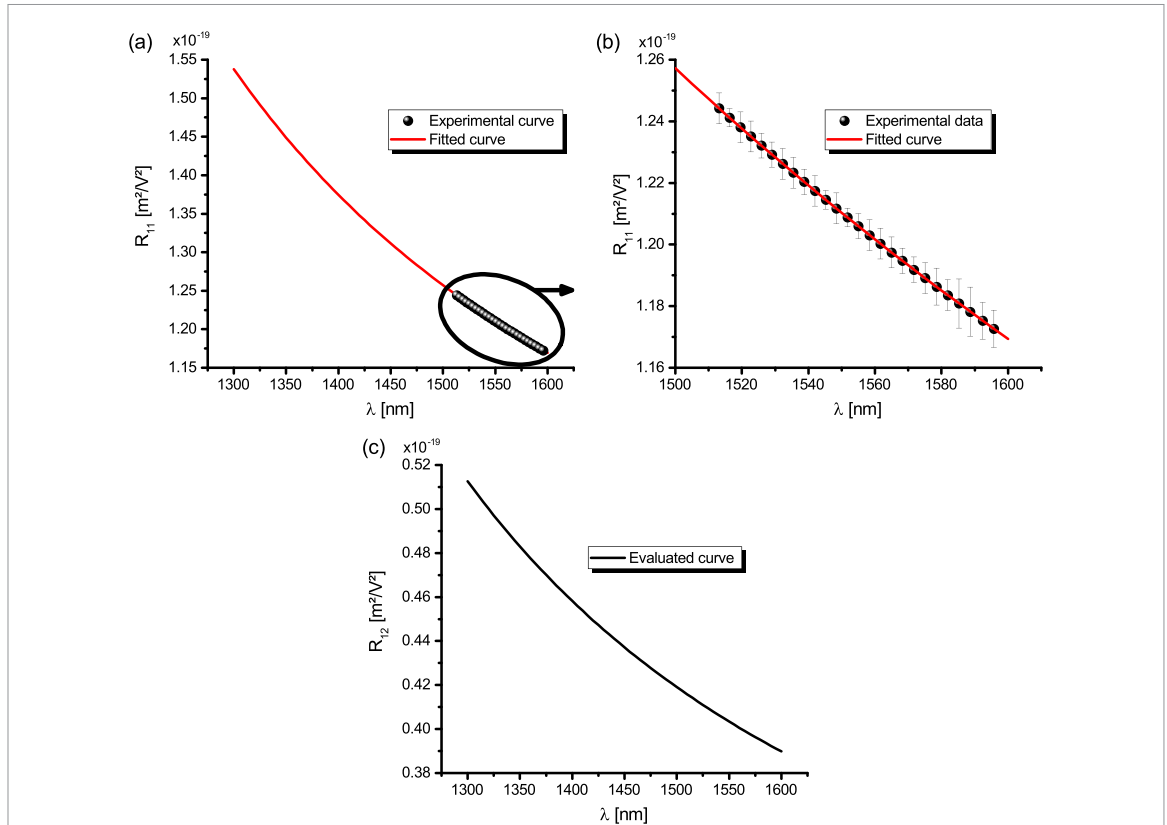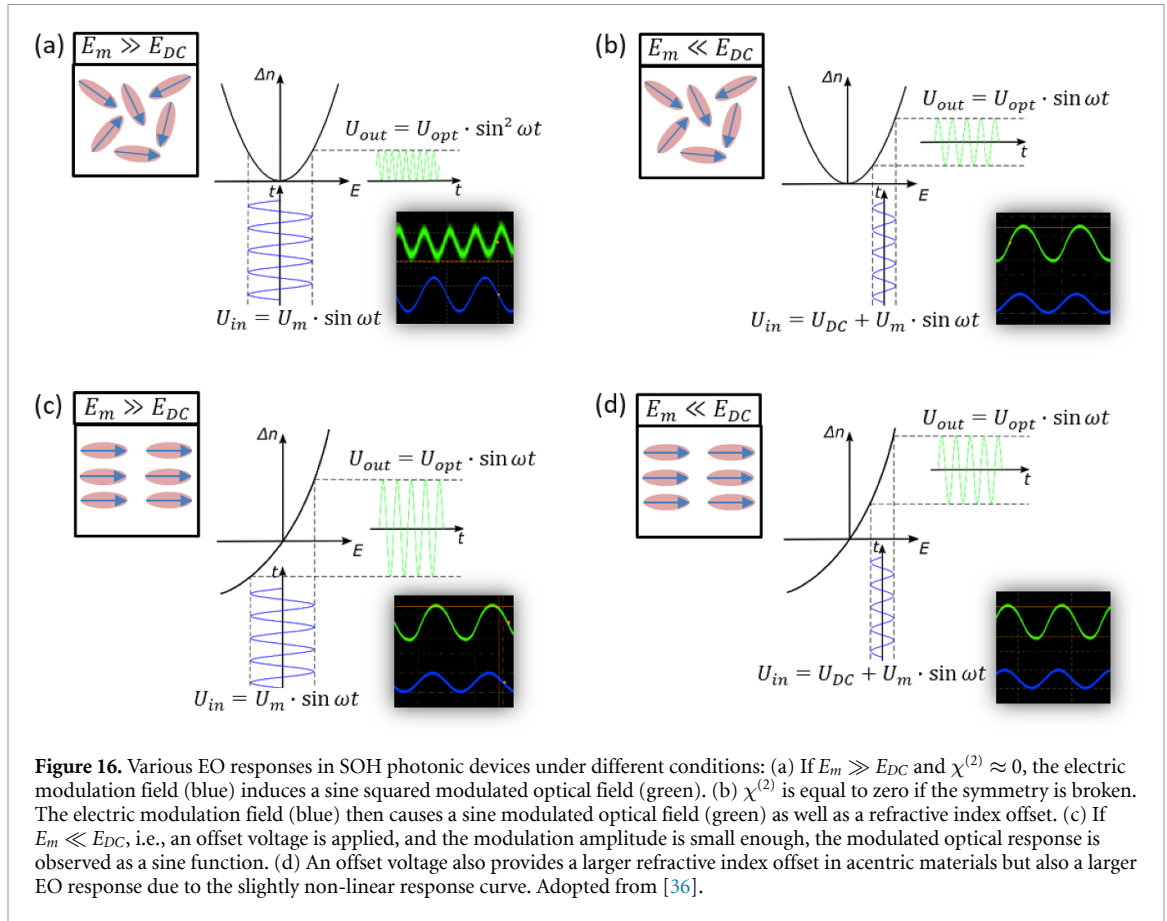
Figure 14. The plotted values of R_{11} in (a) and (b) are observed experimentally and then fitted. The values of R_{12} in (c) are evaluated using the values of R_{11} of (a) by assuming a two-level model and that the electronic mechanisms dominate in the off-resonant spectral region. Adopted from [86].
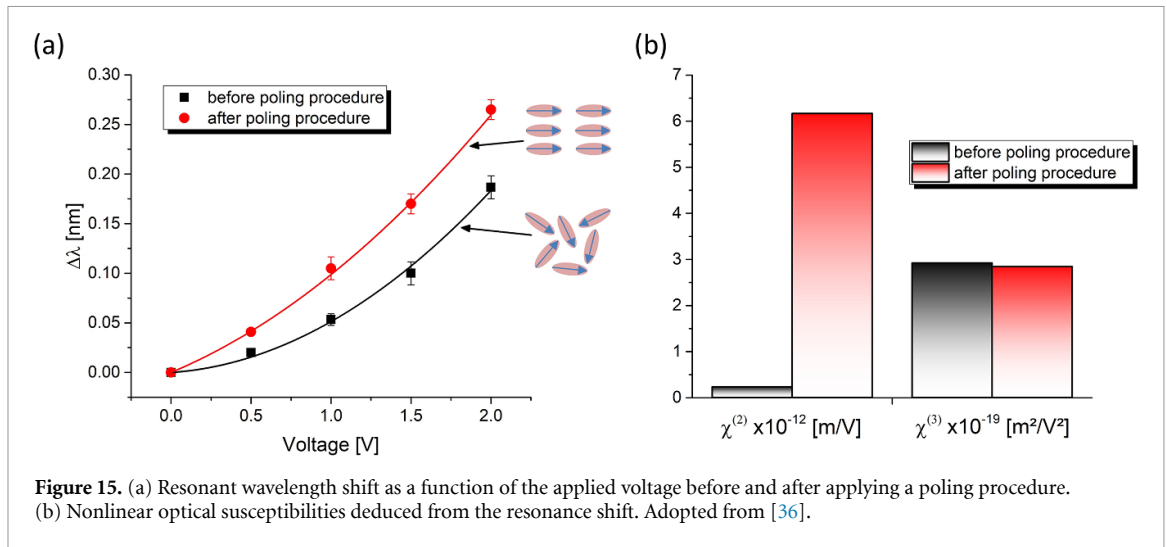
Figure 15. (a) Resonant wavelength shift as a function of the applied voltage before and after applying a poling procedure. (b) Nonlinear optical susceptibilities deduced from the resonance shift. Adopted from [36].

So far, both EO effects have been considered separately, because the quadratic EO effect is significantly weaker compared to the linear EO effect. Classically, the quadratic EO effect is neglected in non-centrosymmetric materials. However, investigations have been undertaken to show that the quadratic EO effect is not only sufficiently strong enough in SOI slot waveguides using a centrosymmetric molecular order, but also contributes to the overall EO effect in non-centrosymmetric materials. In [36], it was revealed that the quadratic EO effect contributes 32% to the overall EO effect. Figure 15(a) shows the experimentally observed resonance wavelength shift of the ring resonator caused by applying an electric field to the SOI slot waveguide. The experiments were performed before and after a poling procedure was applied to the EO material. The non-linear optical susceptibilities are deduced from the curves in figure 15(a) and plotted in figure 15(b). This finding suggests that the overall EO effect should be separated into linear and quadratic contributions to avoid an overestimation of the linear EO coefficient in non-centrosymmetric materials.

Figure 16. Various EO responses in SOH photonic devices under different conditions: (a) If $E_m \gg E_{DC}$ and $\chi^{(2)} \approx 0$, the electric modulation field (blue) induces a sine squared modulated optical field (green). (b) $\chi^{(2)}$ is equal to zero if the symmetry is broken. The electric modulation field (blue) then causes a sine modulated optical field (green) as well as a refractive index offset. (c) If $E_m \gg E_{DC}$, i.e., an offset voltage is applied, and the modulation amplitude is small enough, the modulated optical response is observed as a sine function. (d) An offset voltage also provides a larger refractive index offset in acentric materials but also a larger EO response due to the slightly non-linear response curve. Adopted from [36].

Furthermore, the influence of both EO effects on intensity modulation was investigated in [36]. As shown in figure 16, the simultaneous use of both EO effects can lead to different modulation schemes. This gives rise to novel concepts for reconfigurable and field-programmable photonic devices.

3.4. In-device performance of the electric-field-induced linear electro-optical effect

Silicon also exhibits a relatively large third-order optical susceptibility $\chi^{(3)}$ [148]. Unfortunately, this is accompanied by nonparametric processes such as two-photon absorption (TPA) and free-carrier absorption (FCA) at the optical intensities required in the telecommunications wavelength bands. The heterogeneous integration of materials with high $\chi^{(3)}$ and insignificant TPA and FCA has been pursued to avoid that shortcoming. For example, chalcogenide (ChG) glass [149], Hydex [150], Si_3N_4 [151], and hydrogenated amorphous silicon (*a*-Si:H) [152] are some of the major non-organic materials that have been employed recently.

However, the major advantage of organic materials, compared to silicon, is their negligible nonparametric processes (TPA, FCA). Therefore, third-order non-linear effects are also of great interest in the development of SOH photonic devices. One promising third-order effect in organic materials is the electric-field-induced linear EO effect, which is based on $\chi^{(3)}$ and has been recently revealed in polymers and an SOH ring resonator [153].

It is induced by applying a static electric field in addition to a time-varying (modulated) electric field:

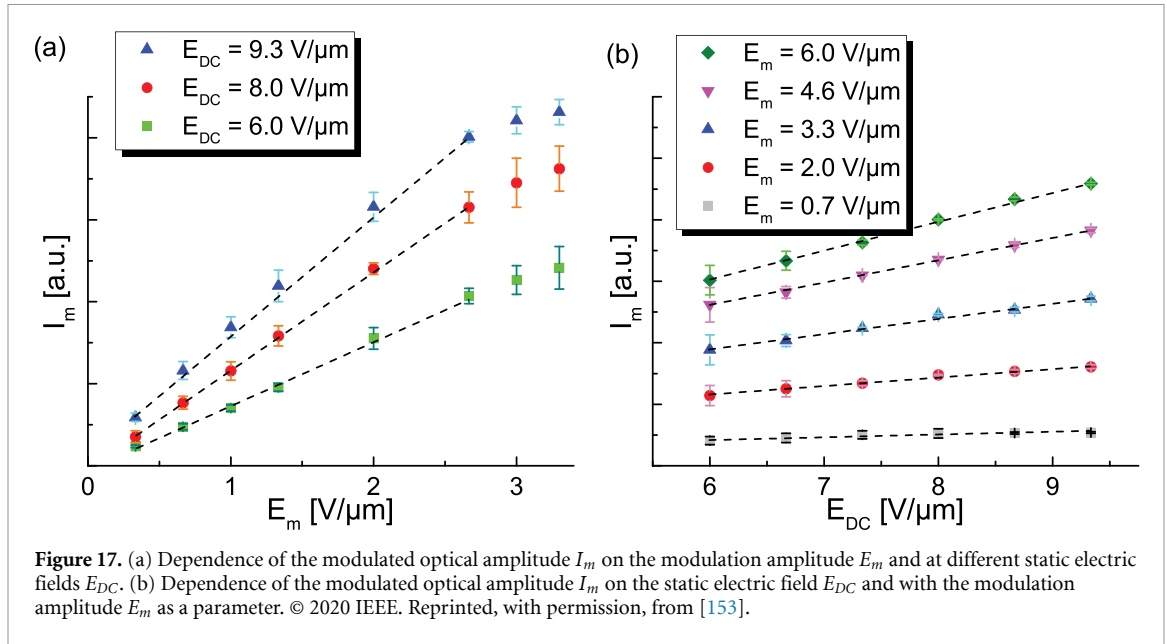$$E = E_{DC} + E_m \sin(\omega t), \tag{8}$$

where E_{DC} is the static electric field and $E_m \sin(\omega t)$ denotes the modulation field. All fields are evaluated by the applied voltage and slot width ($E = U/s$). Inserting equation (8) into the refractive index change (quadratic EO effect):

$$\Delta n = \frac{1}{n} \frac{3}{2} \chi_{3333}^{(3)}(-\omega; \omega, 0, 0) E^2, \tag{9}$$

leads to

$$\Delta n = \frac{3}{2} \frac{\chi^{(3)}}{n} [E_{DC}^2 + E_m^2 \sin^2(\omega t) + 2 E_{DC} E_m \sin(\omega t)]. \tag{10}$$

Figure 17. (a) Dependence of the modulated optical amplitude I_m on the modulation amplitude E_m and at different static electric fields E_{DC}. (b) Dependence of the modulated optical amplitude I_m on the static electric field E_{DC} and with the modulation amplitude E_m as a parameter. © 2020 IEEE. Reprinted, with permission, from [153].

The first term does not influence the EO modulation, since it is a constant. However, it is expedient to distinguish between the two cases. On the one hand, if $E_m \gg E_{DC}$, the third term in equation (10) can be neglected. Consequently, the optical signal follows a sine-squared relation ($E_m^2 \sin^2(\omega t)$). On the other hand, the second term can be neglected and the observed signal is dominated by the third term if $E_m \ll E_{DC}$, which follows a simple sine relation ($2E_{DC}E_m \sin(\omega t)$). This case is referred to as the electric-field-induced linear EO effect. Here, the third-order susceptibility $\chi^{(3)}$ is efficiently translated into an electric-field-induced second-order susceptibility $\chi_{EFI}^{(2)} = 3\chi^{(3)}E_{DC}$ [154].

To validate the electric-field-induced linear EO effect in SOH devices, it is reasonable to distinguish the modulated optical signal in two cases. Here, the measured output intensity (I_{out}) of an optical resonator can be observed as:

$$I_{out} = I_m \sin^2(\omega t) \propto \frac{3\chi^{(3)}}{2n} E_m^2 \sin^2(\omega t), \tag{11}$$

if $E_{DC} \ll E_m$ or

$$I_{out} = I_m \sin(\omega t) \propto \frac{\chi_{EFI}^{(2)}}{n} E_m \sin(\omega t), \tag{12}$$

if $E_{DC} \gg E_m$, where I_m refers to the detected intensity in terms of the modulation amplitude.

First, a sinusoidal input signal $E_m \sin(\omega t)$ is applied without a static electric field, i.e. without an offset voltage, to validate equation (11). In this case, the modulation amplitude is set to a fixed value. In a further experiment, equation (12) is confirmed by applying a static electric field induced by an offset voltage in addition to a modulation amplitude.

One unique feature of the electric-field-induced linear EO effect is the linear dependency of the modulation amplitude E_m on the modulation optical amplitude I_m. Figure 17(a) shows the intensity amplitude, I_m, obtained as a function of the observed amplitude E_m, using different static electric field strengths, E_{DC}. Large modulation fields E_m (>2.8 V μm^{-1}) lead to a non-linear response. As a consequence, only the parameter space in which the modulation is purely linear is fitted in figure 17(a). However, a change of the static electric field strength E_{DC} leads to an increase in the slope of the graph in figure 17(a). Figure 17(b) shows the modulated optical amplitude I_m as a function of the static electric field E_{DC} and the modulated electric field amplitude E_m as a parameter. From this figure, it is apparent that the static electric field E_{DC} has an impact on the modulated optical amplitude I_m. The linear dependence of the optical output amplitude on the static electric field gives rise to novel applications. In particular, this approach is a promising candidate for an EO modulator with adjustable amplitude, or as an optical attenuator that does not require additional photonic components. It is also notable that extremely efficient electric-field-induced second-harmonic generation (EFISH) has recently been demonstrated in an EO polymer [155]. This could be another approach for future SOH photonic devices.
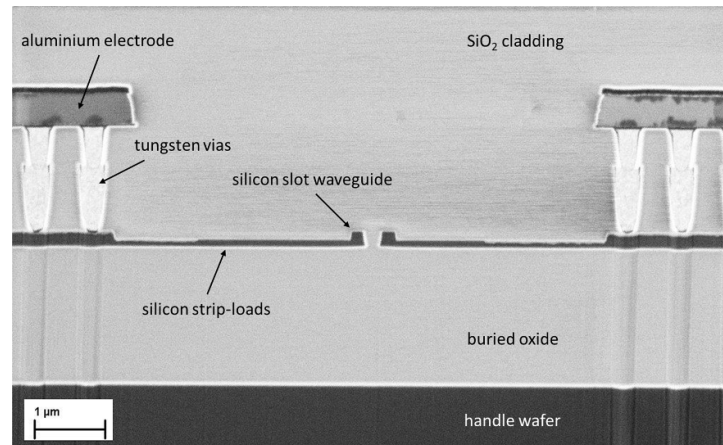
Figure 18. Cross-sectional view (focused ion-beam image) of a strip-loaded slot waveguide in a PIC technology. Adopted from [71].
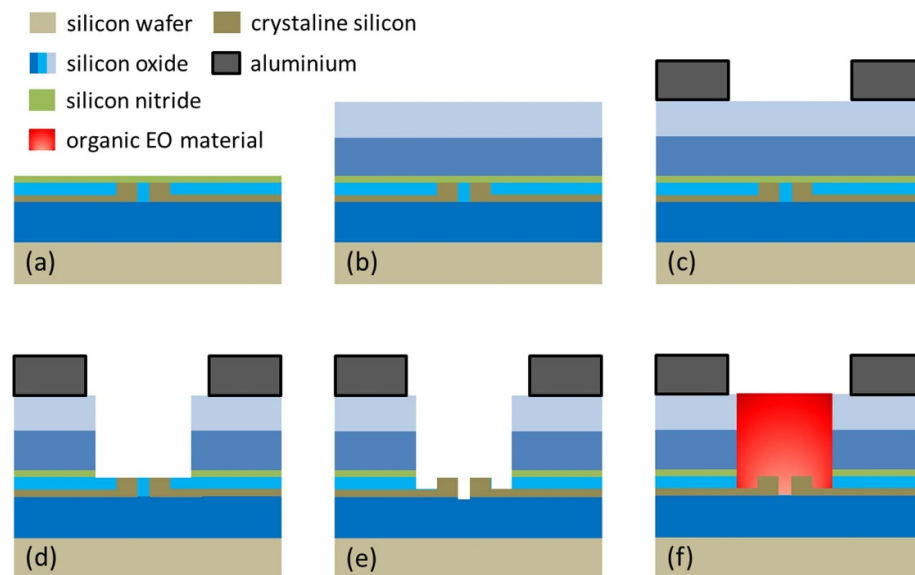

Figure 19. (a) Slot waveguide covered by silicon dioxide and silicon nitride layers with thicknesses of 10 nm and 100 nm, respectively. (b) Back end of line (BEOL) to connect the doped silicon strip loads with the first metal layer and with planarizing silicon dioxide layers after deposition and chemical-mechanical polishing (CMP). (c) First metal layer structured by reactive ion etching (RIE) over a resist mask. (d) RIE up to the silicon nitride sheet (thickness of 50 ± 20 nm) to structure the cavity. (e) Structuring the last part of the cavity by removing the silicon dioxide within the slot using wet etching. (f) Slot waveguide filled with organic material by spin coating. Adopted from [156].

4. Overview of CMOS integration concepts and future aspects

The main challenge for future SOH devices is their integration into CMOS-compatible process flows. The iIndustrial adoption of SOH devices can be achieved using PIC technology. For example, this can be realized as a modular part of a complex SiGe-BiCMOS platform [65, 156]. This technology uses either an SOI wafer or a local SOI on a bulk silicon wafer for the monolithic integration of photonic and electronic devices. Figure 18 shows a focused ion image of a slot waveguide in such a technology. The slot waveguide is connected through doped silicon strip loads and tungsten vias to aluminum electrodes. The slot waveguide needs to be released from the SiO_2-cladding to deposit an EO polymer inside the slot by spin-coating.

Therefore, the process flow is interrupted for simplicity after structuring the first metal layer instead of fabricating the complete back-end of line (BEOL) with five metal layers. To release the silicon slot waveguide, the SiO_2-cladding is locally removed using an etching procedure [156, 157]. The complete release process is schematically shown in figure 19. First, the front-end of the line (FEOL) is finished (figure 19(a)). At this point, the slot waveguide is covered by silicon dioxide and silicon nitride layers with thicknesses of 10 and 100 nm, respectively. The BEOL is fabricated until the first metal layer is the next step, as shown in
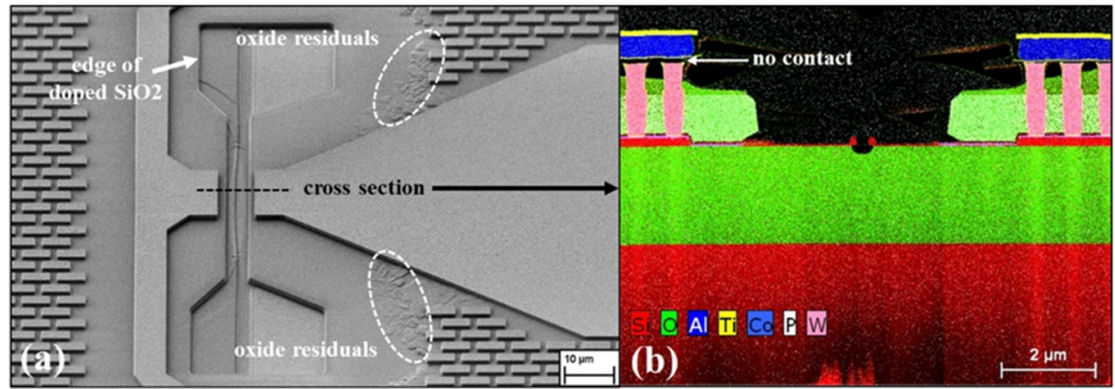
Figure 20. (a) Top and (b) cross-sectional views (focused ion-beam image) of a strip-loaded slot waveguide in PIC technology. Adopted from [71].
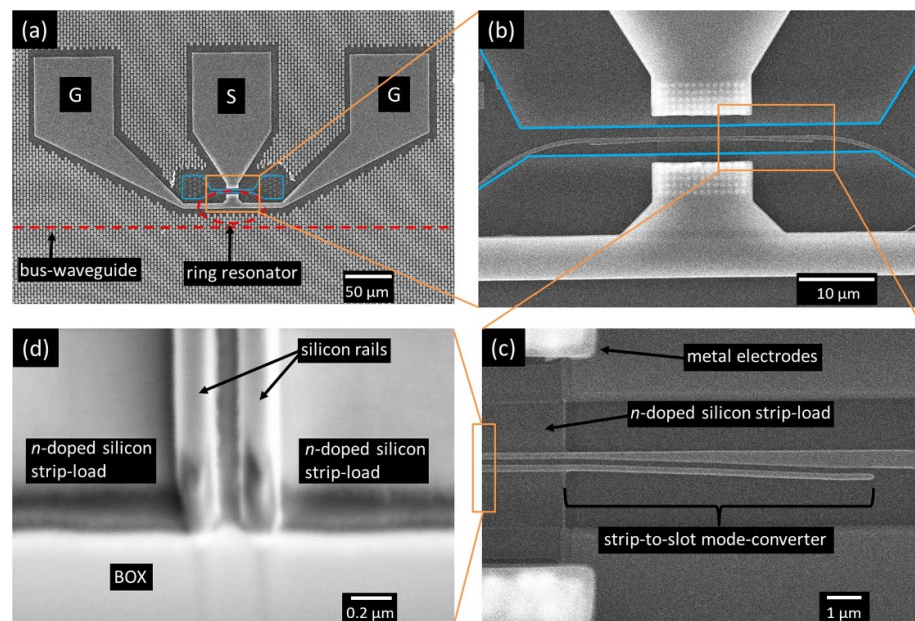
Figure 21. (a) Secondary electron microscopic (SEM) image of the ground–signal–ground electrodes from the above with a trench (highlighted in blue) to deposit the EO polymer inside the silicon slot waveguide. The ring resonator and bus waveguide are shown by a dashed red line. (b) Magnification of the ring resonator with strip-to-slot mode converter and slot waveguide. (c) Magnification of the strip-to-slot mode converter. (d) Details of the strip-loaded silicon slot waveguide. © 2018 IEEE. Reprinted, with permission, from [65].

figures 19(a) and (b). Chemical–mechanical polishing (CMP) steps are employed to get a planar topography of the deposited silicon dioxide layers. The metal electrodes are deposited on top of the silicon dioxide layers and structured by reactive ion etching (RIE) using a hard mask. A further resist mask is used to remove the silicon dioxide stack above the slot waveguide by RIE (figure 19(d)). It turns out that this process step is challenging, because the oxide stack above the wafer has relatively low uniformity in terms of etching speed. Therefore, an RIE process that is very selective to silicon nitride is used to overcome this issue. The silicon dioxide is removed up to the silicon nitride layer. The remaining silicon nitride is etched using RIE with high selectivity to the underlying oxide. Finally, the silicon oxide is removed with a wet-etch process to completely release the slot waveguide (figure 19(e)). The EO polymer is then deposited by spin-coating (figure 19(f)). Further details of the fabrication process can be found in [71, 156, 157]. Figure 20 shows a slot waveguide fabricated in a 0.25 μm SiGe BiCMOS pilot line following the fabrication scheme in figure 19 [65]. It is apparent from this figure that the slot waveguide is completely released. However, the tungsten vias and metal electrodes are partly disconnected because of the relatively long wet-etch procedure, which induces stress due to the missing oxide below the metal electrodes. This, in turn, reduces the device's performance, since the resistance is drastically increased . Further developments are necessary to tackle this problem, which is the subject of ongoing research. However, this technology was first translated into a working device in 2015

and 2016 [32, 94]. In 2018, the first RF modulator was presented using a ring resonator structure, as shown in figure 21 [65].

The integration approach described above allowed the first implementation of EO polymers using a PIC platform based on a CMOS pilot line. However, the main challenge of SOH devices is their compatibility with established foundries. The drawback is the fact that the above-mentioned approach still prohibits the integration of SOH devices with a full BEOL, which is necessary for monolithic integration with electronic circuits. If SOH modulators are to be used in optical communications, they will require tight integration with digital-to-analog converters (DACs). In general, EO modulators require active control and stabilization. This could be solved using electronic control elements that are co-integrated with the photonic devices [158]. One possible solution is the introduction of the EO polymer from the back of the wafer instead of from the front, which is a focus of current research [159–161]. For example, a local back-side release process for introducing organic materials from the back side of the wafer was introduced in 2020 [162, 163]. This approach uses DUV (KrF) and i-line 250 nm CMOS-baseline technology. The back end of line consists of three thin and two thick metal layers. This approach could pave the way for SOH modulators monolithically integrated into electronic-photonic integrated circuits (EPICs), co-integrated with high-performance SiGe hetero-junction bipolar transistors (HBT) [164].

In terms of packaging, the main issue facing SOH photonics is the deposition of the organic material. Since most EO polymers need to be spin-coated onto the chip, the electrodes are covered with the remaining polymer, making a sophisticated cleaning procedure necessary. In principle, the packaging of SOH modulators can be realized by flip-chip or wire bonding [165]. However, attention has to be paid to the temperatures that are necessary for flip-chip bonding. Many EO polymers presented in the literature, such as DLD164 (see [74]), exhibit glass transition temperatures below 70 °C, making them unsuitable for flip-chip bonding because the temperature during this process is usually above 80 °C; therefore, wire bonding at low temperatures is preferable. The first proof of concept of an electrically packaged SOH modulator was demonstrated by Zwickel *et al* [166]. Their SOH modulator was connected through wire bonding to a ceramic printed circuit board (PCB), including RF connectors. In this way, a line rate of 160 Gbit s^{-1} (40 GBd) using 16QAM was demonstrated.

A further challenge to be tackled in future work is that of the photo-induced degradation of EO polymers due to the high intensities inside the slot waveguide. Some studies concluded that the main degradation process can be attributed to the oxidation of the EO polymer [167, 168]. Protection of the organic material by an oxygen-blocking encapsulation has been suggested [119]. By addressing the aforementioned challenges, we are convinced that the industrial adoption of SOH modulators can be realized in the near future.

5. Conclusions

In this work, we have reviewed recent advances in SOH photonics by considering device concepts and material properties. Slot waveguides, the key components of SOH photonics, have been demonstrated with a 3.7 dB cm^{-1} propagation loss [64] and a strip-to-slot mode converter reaching record low losses of about 0.02 dB has been realized on an SOI wafer [66]. Additional fabrication steps such as atomic layer deposition can further decrease propagation losses, which are caused by random line-edge sidewall roughness scattering [59]. With no compromise to signal quality, SOH modulators based on Mach–Zehnder interferometers enable higher-order modulation formats such as 16QAM [75], 8-ASK [80] and PAM4 [77] by employing the linear EO effect (Pockels effect) in organic materials. In addition, SOH modulators based on slotted photonic crystal waveguides have been demonstrated for EO modulation with a 40 GHz 3 dB bandwidth [54]. Recently, the quadratic EO effect [16] and the electric-field-induced linear EO effect [153] have been exploited in polymer-filled slot waveguides, opening perspectives for novel device concepts. Finally, we have provided an overview of recent concepts for integrating organic materials into CMOS technology. A wafer back-side release process has been identified as a promising candidate for the monolithic integration of SOH modulators [162]. In conclusion, SOH photonic devices have been demonstrated as suitable for high-speed modulation with ultra-low energy per bit consumption, and novel CMOS integration concepts offer the prospect of large-scale and cost-effective fabrication of future SOH modulators.

ORCID iD

Patrick Steglich ⬤ https://orcid.org/0000-0002-3689-5737

References

[1] Bogaerts W and Selvaraja S 2014 Silicon-on-insulator (SoI) technology for photonic integrated circuits (PICs) *Silicon-On-Insulator (SOI) Technology* (Amsterdam: Elsevier) pp 395–434

[2] Mai A, Steglich P, Mai C, Simon S and Scholz R 2019 Electronic-photonic wafer-level technologies for fast prototyping and application specific solutions *PhotonIcs Electromagnetics Symp.—Spring (PIERS-Spring)* (Piscataway, NJ: IEEE) pp 249–55

[3] Knoll D *et al* 2015 High-performance photonic BICMOS process for the fabrication of high-bandwidth electronic-photonic integrated circuits *2015 IEEE International Electron Devices Meeting (IEDM)* (Piscataway, NJ: IEEE) pp 15–6

[4] Zimmermann L, Knoll D, Kroh M, Lischke S, Petousi D, Winzer G and Yamamoto Y 2015 BICMOS silicon photonics platform *Optical Fiber Conf.* (Washington, DC: Optical Society of America) p Th4E–5

[5] Thomson D J *et al* 2014 *Laser Photon. Rev.* **8** 180–7

[6] Carroll L *et al* 2016 *Appl. Sci.* **6** 426

[7] Mai A, Bondarenko S, Mai C and Steglich P 2019 Photonic thermal sensor integration towards electronic-photonic-IC technologies *ESSDERC 2019—49th European Solid-State Device Conf. (ESSDERC)* pp 254–7

[8] Lim A E J, Song J, Fang Q, Li C, Tu X, Duan N, Chen K K, Tern R P C and Liow T Y 2014 *IEEE J. Sel. Top. Quantum Electron.* **20** 405–16

[9] Thomson D *et al* 2016 *J. Opt.* **18** 073003

[10] Monroe C, Raussendorf R, Ruthven A, Brown K, Maunz P, Duan L M and Kim J 2014 *Phys. Rev.* A **89** 022317

[11] Kibune M *et al* 2015 A 25 gbps silicon photonic transmitter and receiver with a bridge structure for CPU interconnects *Optical Fiber Conf.* (Washington, DC: Optical Society of America) pp Th1G–2

[12] Alimonti G *et al* 2019 *Nucl. Instrum. Methods Phys. Res.* A **936** 601–3

[13] Steglich P *et al* 2017 *IEEE J. Sens.* **17** 4781–90

[14] Steglich P, Hülsemann M, Dietzel B and Mai A 2019 *Molecules* **24** 519

[15] Reed G T, Mashanovich G, Gardes F and Thomson D 2010 *Nat. Photon.* **4** 518–26

[16] Steglich P, Mai C, Villringer C, Pulwer S, Casalboni M, Schrader S and Mai A 2018 *Opt. Lett.* **43** 3598–601

[17] Leuthold J, Koos C and Freude W 2010 *Nat. Photon.* **4** 535–44

[18] Chen H W, Peters J D and Bowers J E 2011 *Opt. Express* **19** 1455–60

[19] Honardoost A, Abdelsalam K and Fathpour S 2020 *Laser Photon. Rev.* **14** 2000088

[20] Eltes F *et al* 2019 *J. Lightwave Technol.* **37** 1456–62

[21] Wuttig M, Bhaskaran H and Taubner T 2017 *Nat. Photon.* **11** 465–76

[22] Leuthold J *et al* 2009 *Proc. IEEE* **97** 1304–16

[23] Leuthold J *et al* 2013 *IEEE J. Sel. Top. Quantum Electron.* **19** 3401413

[24] Koos C *et al* 2016 *J. Lightwave Technol.* **34** 256–68

[25] Cho M J, Choi D H, Sullivan P A, Akelaitis A J and Dalton L R 2008 *Prog. Polym. Sci.* **33** 1013–58

[26] Dalton L R, Lao D, Olbricht B C, Benight S, Bale D H, Davies J A, Ewy T, Hammond S R and Sullivan P A 2010 *Opt. Mater.* **32** 658–68

[27] Almeida V R, Xu Q, Barrios C A and Lipson M 2004 *Opt. Lett.* **29** 1209–11

[28] Xu Q, Almeida V R, Panepucci R R and Lipson M 2004 *Opt. Lett.* **29** 1626–8

[29] Palmer R *et al* 2013 *IEEE Photon. Technol. Lett.* **25** 1226–9

[30] Weimann C *et al* 2014 *Opt. Express* **22** 3629–37

[31] Pfeifle J *et al* 2014 *Nat. Photon.* **8** 375–80

[32] Steglich P *et al* 2016 *Proc. SPIE* **9891** 98910R

[33] Janjan B, Ahmadi V, Miri M and Fathi D 2020 *J. Opt. Soc. Am.* B **37** 376–81

[34] Korn D *et al* 2016 *Nat. Commun.* **7** 1–9

[35] Chen B *et al* 2018 *Dyes Pigments* **158** 474–81

[36] Steglich P, Mai C, Villringer C and Mai A 2020 *J. Phys. D: Appl. Phys.* **53** 125106

[37] Bogaerts W and Rahim A 2020 *IEEE J. Sel. Top. Quantum Electron.* **26** 1–17

[38] Steglich P 2018 Silicon-on-insulator slot waveguides: theory and applications in electro-optics and optical sensing *Emerging Waveguide Technology* ed K Y You (Rijeka: IntechOpen) ch 10

[39] Robinson J T, Preston K, Painter O and Lipson M 2008 *Opt. Express* **16** 16659–69

[40] Müllner P and Hainberger R 2006 *IEEE Photonics Technol. Lett.* **18** 2557–9

[41] Steglich P, Villringer C, Dümecke S, Michel Y P, Casalboni M and Schrader S 2015 *Design Optimization of Slot-Waveguides Covered with Organic Cladding Materials for Integrated Photonic Devices NWK 16* ed S Middendorf and G Hüttinger (Berliner Wissenschafts-Verlag GmbH) pp 192–8

[42] Steglich P, Villringer C, Dümecke S, Michel Y P, Casalboni M and Schrader S 2015 Silicon-on-insulator slot-waveguide design trade-offs *Proc. 3rd Int. Conf. Photonics, Optics and Laser Technology* pp 47–52

[43] Steglich P, Casalboni M and Schrader S K 2016 Concepts and design of novel integrated photonic devices based on silicon-organic hybrid technology *PHOTOPTICS 2016*

[44] Steglich P, Villringer C, Pulwer S, Casalboni M and Schrader S 2016 Design optimization of silicon-on-insulator slot-waveguides for electro-optical modulators and biosensors *Photoptics 2015 Springer Proceedings in Physics* ed P Ribeiro and M Raposo (Cham: Springer International Publishing) ch 11, pp 173–87

[45] Wang X, Lin C Y, Chakravarty S, Luo J, Jen A K Y and Chen R T 2011 *Opt. Lett.* **36** 882–4

[46] Gao Y, Huang X and Xu X 2014 *Opt. Express* **22** 8765–78

[47] Serna S, Colman P, Zhang W, Le Roux X, Caer C, Vivien L and Cassan E 2016 *Sci. Rep.* **6** 26956

[48] Xia J, Serna S, Zhang W, Vivien L and Éric C 2016 *Photon. Res.* **4** 257–61

[49] Liu B, Wang T, Tang J, Li X, Dong C and He Y 2013 *Appl. Opt.* **52** 8394–401

[50] Chen T, Sun J and Li L 2012 *Opt. Express* **20** 20043–58

[51] Inoue S i and Otomo A 2013 *Appl. Phys. Lett.* **103** 171101

[52] Zhao Y, Zhang Y and Wang Q 2014 *IEEE Trans. Nanotechnol.* **13** 687–94

[53] Wülbern J H, Petrov A and Eich M 2009 *Opt. Express* **17** 304–13

[54] Wülbern J H, Prorok S, Hampe J, Petrov A, Eich M, Luo J, Jen A K Y, Jenett M and Jacob A 2010 *Opt. Lett.* **35** 2753–5

[55] Palmer R *et al* 2014 *J. Lightwave Technol.* **32** 2726–34

[56] Yan H, Xu X, Chung C J, Subbaraman H, Pan Z, Chakravarty S and Chen R T 2016 *Opt. Lett.* **41** 5466–9

[57] Zhang X, Chung C, Hosseini A, Subbaraman H, Luo J, Jen A K, Nelson R L, Lee C Y and Chen R T 2016 *J. Lightwave Technol.* **34** 2941–51

[58] Simili D V and Cada M 2019 *Opt. Express* **27** 26203–17

[59] Alasaarela T, Korn D, Alloatti L, Säynätjoki A, Tervonen A, Palmer R, Leuthold J, Freude W and Honkanen S 2011 *Opt. Express* **19** 11529–38

[60] Säynätjoki A, Karvonen L, Alasaarela T, Tu X, Liow T Y, Hiltunen M, Tervonen A, Lo G Q and Honkanen S 2011 *Opt. Express* **19** 26275–82

[61] Autere A *et al* 2015 *Opt. Express* **23** 26940–51

[62] Ahmadi L, Tervo J, Saarinen J and Honkanen S 2013 *Appl. Opt.* **52** 8089–94

[63] Raza A, Clemmen S, Wuytens P, Muneeb M, Van Daele M, Dendooven J, Detavernier C, Skirtach A and Baets R 2018 *APL Photon.* **3** 116105

[64] Debnath K, Khokhar A Z, Boden S A, Arimoto H, Oo S Z, Chong H M H, Reed G T and Saito S 2016 *Front. Mater.* **3** 51

[65] Steglich P, Mai C, Peczek A, Korndörfer F, Villringer C, Dietzel B and Mai A 2018 Quadratic electro-optical silicon-organic hybrid RF modulator in a photonic integrated circuit technology *2018 IEEE Int. Electron Devices Meeting (IEDM)* (Piscataway, NJ: IEEE) pp 23.3.1–4

[66] Palmer R *et al* 2013 *IEEE J. Photon.* **5** 2200409

[67] Liu Y, Baehr-Jones T, Li J, Pomerene A and Hochberg M 2011 *IEEE Photon. Technol. Lett.* **23** 1496–8

[68] Huang Q *et al* 2009 *Proc. SPIE* **7516** 146–51

[69] Deng Q, Yan Q, Liu L, Li X, Michel J and Zhou Z 2016 *Opt. Express* **24** 7347–55

[70] Han K, Kim S, Wirth J, Teng M, Xuan Y, Niu B and Qi M 2016 *Opt. Express* **24** 6532–41

[71] Steglich P, Mai C, Villringer C, Schrader S and Mai A 2019 *ECS Trans.* **92** 187–94

[72] Deng Q, Liu L, Li X and Zhou Z 2014 *Opt. Lett.* **39** 5665–8

[73] Mere V, Kallega R and Selvaraja S K 2018 *Opt. Express* **26** 438–44

[74] Koeber S *et al* 2015 *Light: Sci. Appl.* **4** e255

[75] Korn D *et al* 2013 *Opt. Express* **21** 13219–27

[76] Palmer R *et al* 2014 High-speed silicon-organic hybrid (SOH) modulators with 230 PM V^{-1} electro-optic coefficient using advanced materials *Optical Fiber Conf.* (Washington, DC: Optical Society of America) p M3G.4

[77] Wolf S *et al* 2018 *Sci. Rep.* **8** 2598

[78] Korn D *et al* 2014 *IEEE J. Photon.* **6** 1–9

[79] Zwickel H *et al* 2017 *Opt. Express* **25** 23784–800

[80] Palmer R *et al* 2013 *IEEE J. Photon.* **5** 6600907

[81] Koos C *et al* 2016 *J. Lightwave Technol.* **34** 256–68

[82] Ding R *et al* 2010 *Opt. Express* **18** 15618–23

[83] Hochberg M, Baehr-Jones T, Wang G, Huang J, Sullivan P, Dalton L and Scherer A 2007 *Opt. Express* **15** 8401–10

[84] Wolf S, Zwickel H, Kieninger C, Lauermann M, Hartmann W, Kutuvantavida Y, Freude W, Randel S and Koos C 2018 *Opt. Express* **26** 220–32

[85] Lauermann M *et al* 2014 *Opt. Express* **22** 29927–36

[86] Steglich P, Villringer C, Dietzel B, Mai C, Schrader S, Casalboni M and Mai A 2019 *IEEE J. Photon.* **11** 1–10

[87] Ding R, Baehr-Jones T, Kim W J, Xiong X, Bojko R, Fedeli J M, Fournier M and Hochberg M 2010 *Opt. Express* **18** 25061–7

[88] Gould M, Baehr-Jones T, Ding R, Huang S, Luo J, Jen A K Y, Fedeli J M, Fournier M and Hochberg M 2011 *Opt. Express* **19** 3952–61

[89] Baehr-Jones T, Hochberg M, Wang G, Lawson R, Liao Y, Sullivan P, Dalton L, Jen A and Scherer A 2005 *Opt. Express* **13** 5216–26

[90] Claes T, Molera J, De Vos K, Schachtb E, Baets R and Bienstman P 2009 *IEEE J. Photon.* **1** 197–204

[91] Dai J, Zhang M, Zhou F, Wang Y, Lu L and Liu D 2015 *Opt. Commun.* **350** 235–40

[92] Zhang W, Serna S, Roux X L, Alonso-Ramos C, Vivien L and Cassan E 2015 *Opt. Lett.* **40** 5566–9

[93] Zhang W, Serna S, Roux X L, Vivien L and Cassan E 2015 Silicon slot waveguide ring resonators: can we target high q factors? *2015 17th Int. Conf. Transparent Optical Networks (ICTON)* pp 1–2

[94] Steglich P *et al* 2015 *IEEE Photon. Technol. Lett.* **27** 2197–200

[95] Xu X, Pan Z, Chung C, Chang C, Yan H and Chen R T 2019 *IEEE J. Sel. Top. Quantum Electron.* **25** 1–8

[96] Pan Z, Xu X, Chung C, Dalir H, Yan H, Chen K, Wang Y, Jia B and Chen R T 2018 *Laser Photonics Rev.* **12** 1700300

[97] Pan Z, Xu X, Chung C J, Dalir H, Yan H, Chen K, Wang Y and Chen R T 2018 High speed modulator based on electro-optic polymer infiltrated subwavelength grating waveguide ring resonator *Optical Fiber Conf.* (Washington, DC: Optical Society of America) p M2I.2

[98] Pan Z, Xu X, Chung C J, Dalir H, Yan H, Chen K, Wang Y, Jia B and Chen R T 2018 High-speed silicon-organic hybrid modulator enabled by sub-wavelength grating waveguide ring resonator *Conf. Lasers and Electro-Optics* (Washington, DC: Optical Society of America) p SM1I.2

[99] Pan Z, Xu X, Chung C J, Dalir H, Yan H, Chen K, Wang Y, Jia B and Chen R T 2018 *Laser Photon. Rev.* **12** 1700300

[100] Heni W *et al* 2017 *Opt. Express* **25** 2627–53

[101] Michelotti F, Toussaere E, Levenson R, Liang J and Zyss J 1996 *J. Appl. Phys.* **80** 1773–8

[102] Zhang X, Lu X, Wu L and Chen R T 2002 *Proc. SPIE* **4653** 87–95

[103] Kajzar F, Lee K S and Jen A K Y 2003 Polymeric materials and their orientation techniques for second-order nonlinear optics *Polymers for Photonics Applications II* (Berlin: Springer) pp 1–85

[104] Hill R A, Knoesen A and Mortazavi M A 1994 *Appl. Phys. Lett.* **65** 1733–5

[105] Palazzesi C, Stella F, De Matteis F and Casalboni M 2010 *J. Appl. Phys.* **107** 113101

[106] Apostoluk A, Fiorini-Debuisschert C and Nunzi J M 2002 11—all optical poling in polymers and applications *Photoreactive Organic Thin Films* ed Z Sekkat and W Knoll (San Diego, CA: Academic) pp 331–63

[107] Sullivan P A *et al* 2007 *J. Am. Chem. Soc.* **129** 7523–30

[108] Michelotti F, Nicolao G, Tesi F and Bertolotti M 1999 *Chem. Phys.* **245** 311–26

[109] Choi D H, Park J H, Lee J H and Lee S D 2000 *Thin Solid Films* **360** 213–21

[110] Heni W *et al* 2019 *Nat. Commun.* **10** 1694

[111] Xu H, Elder D L, Johnson L E, Robinson B H and Dalton L R 2019 *ACS Appl. Mater. Interfaces* **32** 1408–21

[112] Villringer C, Gilani T S, Zhang E, Pulwer S, Steglich P, Schrader S and Laufer J 2019 *Proc. SPIE* **10878** 28–33

[113] Koos C *et al* 2017 *Proc. SPIE* **10098** 1009807

[114] Dalton L R, Günter P, Jazbinsek M, Kwon O P and Sullivan P A 2015 *Organic Electro-Optics and Photonics: Molecules, Polymers and Crystals* 1st edn (Cambridge: Cambridge University Press)

[115] Kajzar F, Lee K S and Jen A K Y 2003 *Polymeric Materials and their Orientation Techniques for Second-Order Nonlinear Optics* (Berlin: Springer) pp 1–85
[116] Yesodha S K, Pillai C K S and Tsutsumi N 2004 *Prog. Polym. Sci.* **29** 45–74
[117] Haffner C *et al* 2017 *Opt. Mater. Express* **7** 2168–81
[118] Lauermann M *et al* 2016 *Opt. Express* **24** 11694–707
[119] Kieninger C *et al* 2018 *Opt. Express* **26** 27955–64
[120] Jin W *et al* 2014 *Appl. Phys. Lett.* **104** 243304
[121] De Matteis F 2007 *Ferroelectrics* **352** 3–11
[122] Xu H, Liu F, Elder D L, Johnson L E, de Coene Y, Clays K, Robinson B H and Dalton L R 2020 *Chem. Mater.* **32** 1408–21
[123] Qiu F, Miura H, Spring A M, Hong J, Maeda D, Ozawa M a, Odoi K and Yokoyama S 2016 *Appl. Phys. Lett.* **109** 173301
[124] Deng G, Xu H, Zhou Z, Zhao Z, Wu J, Zhang X, Sun K, Li Z and Zheng Y 2019 *Dyes Pigments* **164** 97–104
[125] Hermans A *et al* 2017 *Sci. Rep.* **7** 44581
[126] Kieninger C *et al* 2020 SOH Mach–Zehnder modulators for 100 gbd PAM4 signaling with sub-1 DB phase-shifter loss *Optical Fiber Conf. (OFC) 2020* (Washington, DC: Optical Society of America) p Th3C.3
[127] Kieninger C *et al* 2018 *Optica* **5** 739–48
[128] Wolf S *et al* 2017 Silicon-organic hybrid (SOH) IQ modulator for 100 gbd 16QAM operation *Optical Fiber Conf.* (Washington, DC: Optical Society of America) pp Th5C–1
[129] Kieninger C *et al* 2017 Record-high in-device electro-optic coefficient of 359 PM/V in a silicon-organic hybrid (SOH) modulator *Conf. Lasers and Electro-Optics* (Washington, DC: Optical Society of America) p STu3N.2
[130] Kieninger C *et al* 2017 Record-high in-device electro-optic coefficient of 359 PM/V in a silicon-organic hybrid (SOH) modulator *2017th Conf. Lasers and Electro-Optics (CLEO)* pp 1–2
[131] Zwickel H *et al* 2017 100 gbit/s serial transmission using a silicon-organic hybrid (SOH) modulator and a duobinary driver IC *Optical Fiber Conf. and Exhibition (OFC) 2017* (Piscataway, NJ: IEEE) pp 1–3
[132] Lauermann M *et al* 2016 *Opt. Express* **24** 9389–96
[133] Melikyan A *et al* 2015 *Opt. Express* **23** 9938–46
[134] Alloatti L *et al* 2014 *Light: Sci. Appl.* **3** e173
[135] Schindler P C *et al* 2014 Ultra-short silicon-organic hybrid (SOH) modulator for bidirectional polarization-independent operation *2014 European Conference on Optical Communication (ECOC)* (Piscataway, NJ: IEEE) pp 1–3
[136] Alloatti L *et al* 2013 *Proc. SPIE* **8629** 86290P
[137] Qasymeh M, Cada M and Ponomarenko S A 2008 *IEEE J. Quantum Electron.* **44** 740–6
[138] Kuzyk M G, Sohn J E and Dirk C W 1990 *J. Opt. Soc. Am.* B **7** 842–58
[139] Poga C, Kuzyk M G and Dirk C W 1994 *J. Opt. Soc. Am.* B **11** 80–91
[140] Zheng X, Deng X, Cao Z, Shen Q, Li H, Wei W and Liu F 2009 *IEEE J. Quantum Electron.* **45** 542–6
[141] Herold M, Schmid W, Vogtmann T, Fischer R, Haarer D and Schwoerer M 1995 *Appl. Opt.* **34** 996–1002
[142] Oldroyd A, Mann S and McCallion K 1989 *Electron. Lett.* **25** 1476–7
[143] Kuzyk M G and Dirk C W 1989 *Appl. Phys. Lett.* **54** 1628–30
[144] Bondarenko S, Villringer C and Steglich P 2018 *Appl. Sci.* **9** 89
[145] Harrison M G, Möller S, Weiser G, Urbasch G, Mahrt R F, Bässler H and Scherf U 1999 *Phys. Rev.* B **60** 8650–8
[146] Hu C, Tian H, Yao B, Zhou Z and Chen D 2013 *Curr. Appl. Phys.* **13** 785–8
[147] Vitale F *et al* 2020 *Mater. Res. Proc.* **16** 27–37
[148] Timurdogan E, Poulton C V, Byrd M and Watts M 2017 *Nat. Photon.* **11** 200
[149] Lamont M R, Luther-Davies B, Choi D Y, Madden S and Eggleton B J 2008 *Opt. Express* **16** 14938–44
[150] Moss D J, Morandotti R, Gaeta A L and Lipson M 2013 *Nat. Photon.* **7** 597
[151] Okawachi Y, Yu M, Cardenas J, Ji X, Klenner A, Lipson M and Gaeta A L 2018 *Opt. Lett.* **43** 4627–30
[152] Della Corte F G, Rao S, Coppola G and Summonte C 2011 *Opt. Express* **19** 2941–51
[153] Steglich P, Villringer C,, Dietzel B, Mai C, Schrader S, Casalboni M and Mai A 2020 *IEEE Photon. Technol. Lett.* **32** 526–9
[154] Sutherland R L 2003 *Handbook of Nonlinear Optics* (New York: CRC Press)
[155] Chen S, Li K F, Li G, Cheah K W and Zhang S 2019 *Light: Sci. Appl.* **8** 1–6
[156] Steglich P, Mai C and Mai A 2019 *ECS J. Solid State Sci. Technol.* **8** Q217–Q221
[157] Steglich P *et al* 2019 Functionalized materials for integrated photonics: hybrid integration of organic materials in silicon-based photonic integrated circuits for advanced optical modulators and light-sources *2019 PhotonIcs Electromagnetics Symp.—Spring (PIERS-Spring)* pp 3019–27
[158] Atabaki A H *et al* 2018 *Nature* **556** 349–54
[159] Mai C, Steglich P and Mai A 2019 Adjustment of the BEOL for back side module integration on wafer level in a silicon photonic technology *MikroSystemTechnik 2019; Congress* pp 1–4
[160] Bondarenko S, Steglich P, Schrader S and Mai A 2019 Simulation study of released silicon-on-insulator slot waveguides in a photonic integrated circuit technology *2019 PhotonIcs Electromagnetics Symp.—Spring (PIERS-Spring)* pp 3334–7
[161] Steglich P, Mai A, Mai C and Schrader S 2019 Electrooptical device US Patent App 16/222,301
[162] Mai C, Steglich P, Fraschke M and Mai A 2020 *IEEE Trans. Compon. Hybrids Manuf. Technol.* **10** 1569–74
[163] Steglich P, Bondarenko S, Mai C, Paul M, Weller M and Mai A 2020 *IEEE Photonics Technol. Lett.* **32** 1241–4
[164] Rahim A *et al* 2019 *IEEE J. Sel. Top. Quantum Electron.* **25** 1–18
[165] Bogaerts W and Chrostowski L 2018 *Laser Photon. Rev.* **12** 1700237
[166] Zwickel H, Kemal J N, Kieninger C, Kutuvantavida Y, Rittershofer J, Lauermann M, Freude W, Randel S and Koos C 2018 *Opt. Express* **26** 34580–91
[167] Dinu R *et al* 2009 *J. Lightwave Technol.* **27** 1527–32
[168] Min-Cheol O *et al* 2001 *IEEE J. Sel. Top. Quantum Electron.* **7** 826–35